Extreme Mechanics Letters 54 (2022) 101773

Contents lists available at ScienceDirect

Extreme Mechanics Letters

journal homepage: www.elsevier.com/locate/eml

Large viscoelastic deformation of hard-magnetic soft beams

Farzam Dadgar-Rad [a], Mokarram Hossain [b,*]

[a] Faculty of Mechanical Engineering, University of Guilan, Rasht, Iran
[b] Zienkiewicz Centre for Computational Engineering (ZCCE), Faculty of Science and Engineering, Swansea University, SA1 8EN, UK

ARTICLE INFO

Article history:
Received 8 February 2022
Accepted 4 May 2022
Available online 13 May 2022

Keywords:
Hard-magnetic soft materials
Magneto-active polymers
Viscoelasticity
Magneto-elasticity
Finite deformations
Finite element method

ABSTRACT

This work aims at developing a viscoelastic formulation for the time-dependent finite deformation analysis of beams made of hard-magnetic soft materials (HMSMs) under magnetic loading. After introducing the basic kinematic quantities, a viscoelasticity formulation for the analysis of HMSMs is developed, which is general in the sense that it can be used for 2D and 3D geometries beside the beam, plate, and shell-type structures. Next, the expression for the consistent fourth-order tangent tensors for 3D bodies and beams made of HMSMs are presented. Due to the highly nonlinear nature of the governing equations, a finite element formulation for the numerical solution of beam problems with various loading and boundary conditions is developed. To demonstrate the applicability of the developed formulation, several numerical examples are provided. It is observed that for the case of elastic deformations, the results of the present formulation are very close to those previously reported in the literature. For the case of viscoelastic deformations, the creep response of beams is simulated and the effect of viscoelastic parameters is studied. It is shown that the obtained results are qualitatively in agreement with the basic properties of viscoelastic deformations.

1. Introduction

Magneto-active polymers (MAPs) are a class of soft active composite materials that consist of micron-sized magnetizable particles embedded into an elastomer matrix and exhibit mechanical deformation under magnetic stimuli. These materials have found various applications, e.g., in sensors, remote-controlled soft robotics, smart vibration absorbers, tunable stiffness actuators, and soft and flexible electronics [1–10]. Two different kinds of particles, namely magnetically-soft and magnetically-hard ones are used in MAPs [11–14]. The main characteristic of magnetically-soft particles, such as carbonyl iron, is that they have negligible hysteresis, and their magnetization vector changes by applying magnetic loadings. A short list of researches on the MAPs composed of magnetically-soft particles includes [15–22]. Reviews of the research work on magnetically-soft MAPs are available in [23,24] while Lucarini et al. [25] particularly reviewed hard-magnetic soft materials taking into account their wide range of potential applications. On the other hand, magnetically-hard particles, such as $CoFe_2O_4$ or NdFeB, exhibit significant magnetic hysteresis and their magnetization vector remains constant for a wide range of magnetic loading [26–29]. A magneto-active polymer composed of the latter class of particles is called a hard-magnetic soft material (HMSM). The purpose of this work is to develop mathematical formulations that can capture the time-dependent responses of HMSMs.

Recently, the manufacture and analysis of HMSMs have received considerable attention in science and industry communities. In particular, advanced additive manufacturing (3D printing) technologies have allowed researchers to program the local orientation of the magnetized particles to generate complex deformed shapes under magnetic loads [30–37]. A continuum theory for the finite elastic deformation of HMSMs was developed by Zhao et al. [26]. They then implemented the formulation as a user-element subroutine into the commercial finite element package ABAQUS and analyzed the large deformation of hard-magnetic soft (HMS) beams both numerically and experimentally. Very recently, viscoelastic deformation of HMSMs has been formulated in [38,39]. A micromechanics approach through the representative volume element simulations was also proposed in [40]. Additionally, microstructure-based models accounting for viscous dissipation as well as dipole–dipole interactions were developed in [41,42]. A further microstructural lattice model for HMSMs by partitioning the elastic deformation energy into lattice stretching and volumetric change has been also proposed by [43].

In addition to the constitutive modeling of HMSMs, several research articles dealing with the elastic deformation of HMS beams have been published in the literature. In particular, [34,44] developed analytical and finite difference solutions for finite bending of HMS cantilevers. For instance, in a series of

* Corresponding author.
E-mail addresses: dadgar@guilan.ac.ir (F. Dadgar-Rad), mokarram.hossain@swansea.ac.uk (M. Hossain).

https://doi.org/10.1016/j.eml.2022.101773

papers, Chen and coworkers [45–48] investigated two- and three-dimensional deformations of HMS cantilevers accounting for variable residual magnetic fluxes or variable volume fractions of magnetic particles along the beam. An HMS beam formulation accounting for the antielastic bending effect was proposed in [49]. Moreover, bifurcation analysis of HMS cantilevers under various angles of the applied magnetic flux vector was studied in [50]. A three-dimensional beam formulations for slender HMSMs was developed in [51,52]. They investigated the finite deformation of cantilevers and coils under the application of constant as well as constant gradient magnetic loading both numerically and experimentally.

The aforementioned detailed review of the state-of-the-art research works published in the literature reveals that viscous effects on beams made of HMSMs have not been taken into account. Therefore, the main contribution of this work is to develop a formulation that combines viscoelasticity with the finite deformation of HMS beams under the application of magnetic stimuli. Moreover, a general nonlinear finite element formulation is developed that can be used for arbitrary hyperelastic constitutive equations corresponding to the mechanical contribution of the free energy density function.

The outline of this paper is as follows. In Section 2, kinematics of a deforming HMS beam is formulated. In Section 3, a viscoelastic formulation for the time-dependent response of 3D hard-magnetic soft materials is developed and is specialized to HMS beams. In Section 4, a nonlinear finite element formulation in the Lagrangian framework is derived. To investigate the performance of the developed formulation, several numerical examples are solved and discussed in Section 5. Finally, a summary of the work is provided in Section 6.

2. Kinematics of deformation

Notation: Throughout this work, Greek indices run over {1, 2} and lower-case Latin indices range over {1, 2, 3}. Upper-case Latin indices do not obey a general rule and take the values specified in the corresponding equations. Unless otherwise stated, the summation convention holds over all repeated lower-case Latin indices. An asterisk * is used for the tensor quantities defined in the three-dimensional space. Tensor quantities without an asterisk are defined in the two-dimensional space. For the two second-order tensors $\mathbf{P}^*$ and $\mathbf{Q}^*$, in the three-dimensional space, the fourth-order tensors $\boldsymbol{\mathcal{A}}^* = \mathbf{P}^* \otimes \mathbf{Q}^*$ and $\boldsymbol{\mathcal{B}}^* = \mathbf{P}^* \boxtimes \mathbf{Q}^*$ are defined so that their components are given by $\mathcal{A}^*_{ijkl} = P^*_{ij}Q^*_{kl}$ and $\mathcal{B}^*_{ijkl} = P^*_{il}Q^*_{kj}$, respectively. The double contraction operation on tensors of different orders is defined by $\mathbf{P}^* : \mathbf{Q}^* = P^*_{ij}Q^*_{ij}$, $(\boldsymbol{\mathcal{A}}^* : \mathbf{P}^*)_{ij} = \mathcal{A}^*_{ijpq}P^*_{pq}$, $(\boldsymbol{\mathcal{A}}^* : \boldsymbol{\mathcal{B}}^*)_{ijkl} = \mathcal{A}^*_{ijpq}\mathcal{B}^*_{pqkl}$. The complete inner product of two fourth-order tensors is defined by $\boldsymbol{\mathcal{A}}^* :: \boldsymbol{\mathcal{B}}^* = \mathcal{A}^*_{ijkl}\mathcal{B}^*_{ijkl}$. The notations $\mathbf{P}^{*\top}$, $\mathrm{tr}\,\mathbf{P}^*$, $\det\mathbf{P}^*$ and $\mathbf{P}^{*-1}$ are the transpose, trace, determinant and inverse of the second-order tensor $\mathbf{P}^*$. Moreover, the magnitude of a vector, say $\mathbb{B}^*$, is denoted by $|\mathbb{B}^*|$. It is noted that similar operations and quantities can be defined in the two-dimensional space, e.g., $\mathbf{P} : \mathbf{Q} = P_{\alpha\beta}Q_{\alpha\beta}$.

A straight beam of the length L and variable cross-section, as shown in Fig. 1, is considered. Two coincident Cartesian coordinate systems $\{X_1, X_2, X_3\}$ and $\{x_1, x_2, x_3\}$ are located at the geometric center of the left end of the beam. The basis vectors of both coordinate systems are denoted by $\{\mathbb{e}_1, \mathbb{e}_2, \mathbb{e}_3\}$. The X_2-axis is directed along with the thickness of the beam, and due to the two-dimensional nature of deformation in the X_1X_2-plane, it is assumed that the beam cross-section is symmetric with respect to this axis. The X_3-axis is perpendicular to the plane of deformation and has not been shown in the figure. As usual, the material coordinate system $\{X_1, X_2, X_3\}$ describes the undeformed geometry,

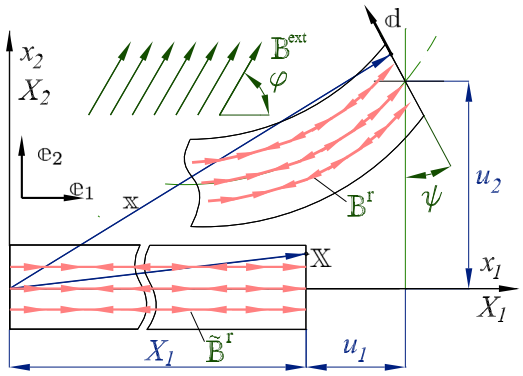

Fig. 1. Schematic view of the deformation of a HMS beam under the uniform external magnetic field $\mathbb{B}^{\text{ext}}$.

while the spatial coordinate system $\{x_1, x_2, x_3\}$ is employed to describe the deformed beam.

The residual magnetic flux density on the undeformed beam is denoted by $\tilde{\mathbb{B}}^{\text{r}}$. The external magnetic flux density $\mathbb{B}^{\text{ext}}$, which makes an angle φ with the X_1-axis, is applied to the beam. Following [26,35,44–50], it is assumed that the external magnetic flux density is uniform in space, and the referential residual magnetic flux density $\tilde{\mathbb{B}}^{\text{r}}$ is parallel to the X_1-axis. It is noted that the magnitude of $\tilde{\mathbb{B}}^{\text{r}}$ may change along the X_1-axis, however, the unit vector along its direction may be $\mathbb{e}_1$ or $-\mathbb{e}_1$. The residual magnetic flux density $\mathbb{B}^{\text{r}}$ on the deformed beam is considered to be tangent to the deformed centerline, and the permeability of the beam is approximated by that of the free space.

Under the assumptions described above, Zhao et al. [26] showed that the Maxwell equations of the form (see, e.g., [53])

$$\mathrm{Curl}\mathbb{H} = \mathbf{0}, \quad \mathrm{Div}\mathbb{B} = \mathbf{0}, \tag{1}$$

are satisfied in HMSMs. Here, $\mathbb{H}$ and $\mathbb{B}$ are the referential magnetic field and the magnetic flux density, respectively. Moreover, Curl and Div are the curl and divergence operators in the reference configuration.

In this work, to describe the kinematics of deformation, the following 3-parameter mapping is considered (e.g., [54,55]):

$$\mathbb{x} = \hat{\mathbb{x}}(\mathbb{X}, t) = \mathbb{x}_0(X_1, t) + X_2\mathbb{d}(X_1, t), \quad \mathbb{d} = -\sin\psi\,\mathbb{e}_1 + \cos\psi\,\mathbb{e}_2, \tag{2}$$

where $\mathbb{x}_0$ and $\mathbb{d}$ are the position vector on the deformed centerline and the director vector, respectively. The director $\mathbb{d}$ is a unit vector obtained by the rotation ψ of the beam cross-section about the X_3-axis. Motivated by the motion field, the centerline displacement vector $\mathbb{u}$ is defined as $\mathbb{u} = \mathbb{x}_0 - \mathbb{X}_0 = u_\alpha\mathbb{e}_\alpha$, where $\mathbb{X}_0 = X_1\mathbb{e}_1$ is the initial position vector of the material points on the undeformed centerline. It is noted that the functions $\{u_1, u_2, \psi\}$ are the three unknown parameters of the present beam formulation. From Eq. (2) the deformation gradient tensor $\mathbf{F}$, in the X_1X_2 plane, may be written as

$$\mathbf{F} = \mathrm{Grad}\mathbb{x} = \frac{\partial x_\alpha}{\partial X_\beta}\mathbb{e}_\alpha \otimes \mathbb{e}_\beta = \mathbf{F}^{(0)} + X_2\mathbf{F}^{(1)}, \tag{3}$$

where the second-order tensors $\mathbf{F}^{(0)}$ and $\mathbf{F}^{(1)}$ are given by

$$\left.\begin{aligned}\mathbf{F}^{(0)} &= (1+u_1')\mathbb{e}_1 \otimes \mathbb{e}_1 - \sin\psi\,\mathbb{e}_1 \otimes \mathbb{e}_2 \\ &\quad + u_2'\mathbb{e}_2 \otimes \mathbb{e}_1 + \cos\psi\,\mathbb{e}_2 \otimes \mathbb{e}_2 \\ \mathbf{F}^{(1)} &= -\psi'(\cos\psi\,\mathbb{e}_1 \otimes \mathbb{e}_1 + \sin\psi\,\mathbb{e}_2 \otimes \mathbb{e}_1)\end{aligned}\right\}. \tag{4}$$

It is noted that the notation $\{\bullet\}' = \partial\{\bullet\}/\partial X_1$ is used throughout the paper. From Eq. (4), the determinant of the deformation gradient is given by

$$J = \det \mathbf{F} = J^{(0)} + X_2 J^{(1)} \quad \text{with} \quad J^{(0)} = \det \mathbf{F}^{(0)} \quad \text{and} \quad J^{(1)} = -\psi'. \tag{5}$$

For later use, the quantities J^{-1}, J^{-2}, and $\mathbf{F}^{-\top}$ are approximated in the following forms:

$$J^{-1} \approx \tilde{J}^{(0)} + X_2 \tilde{J}^{(1)}, \quad J^{-2} \approx \hat{J}^{(0)} + X_2 \hat{J}^{(1)}, \quad \mathbf{F}^{-\top} \approx \tilde{\mathbf{F}}^{(0)} + X_2 \tilde{\mathbf{F}}^{(1)}, \tag{6}$$

where $\tilde{J}^{(I)}$, $\hat{J}^{(I)}$, and $\tilde{\mathbf{F}}^{(I)}$ $(I = 0, 1)$ are given by

$$\left.\begin{aligned} \tilde{J}^{(0)} &= J^{(0)-1}, \quad \tilde{J}^{(1)} = -J^{(0)-2} J^{(1)}, \quad \hat{J}^{(0)} = J^{(0)-2} \\ \hat{J}^{(1)} &= -2J^{(0)-3} J^{(1)}, \quad \tilde{\mathbf{F}}^{(0)} = \mathbf{F}^{(0)-\top}, \quad \tilde{\mathbf{F}}^{(1)} = -\tilde{\mathbf{F}}^{(0)} \mathbf{F}^{(1)\top} \tilde{\mathbf{F}}^{(0)} \end{aligned}\right\}. \tag{7}$$

The kinematic quantities defined in this section will be employed in the subsequent developments.

3. A viscoelasticity formulation for hard-magnetic soft materials

One of the most well-known viscoelasticity theories, widely used in the literature and Finite Element (FE) packages, has been developed by Simo [56]. In this section, a simple generalization of Simo's theory to model hard-magnetic soft materials is developed. In the first step, a viscoelasticity formulation for three-dimensional HMSMs is developed. In the next step, the formulation is specialized to HMS beams.

3.1. Viscoelasticity formulation for HMSMs in 3-space

To start the formulation for the three-dimensional viscoelastic HMSMs, a rheological model as displayed in Fig. 2 is considered. Basically, a magnetic branch is added to the traditional generalized Maxwell model with a single elastic equilibrium branch and N_v viscoelastic ones. Let K^∞ be the stiffness of the equilibrium branch, and K_I^e and η_I be the stiffness and damping of the I'th viscoelastic one, respectively. As has been shown on Fig. 2, $u(t)$ is the total displacement of the system, and $\alpha_I(t)$ $(I = 1, 2, \ldots, N_v)$ denotes the displacement of dampers. From the figure, the total force P acting on the rheological model is given by

$$P = P^{\text{Mag}} + P^\infty + \sum_{I=1}^{N_v} P_I^e = P^{\text{Mag}} + P^{e0} - \sum_{I=1}^{N_v} Q_I, \tag{8}$$

where P^{Mag} is the magnetic force, $P^\infty = K^\infty u$ is the force on the pure elastic branch, $P_I^e = K_I^e(u - \alpha_I) = K_I^e u - Q_I$ is the force on the I'th viscoelastic branch, and $Q_I = K_I^e \alpha_I$ is considered to be the internal variable of the formulation. Moreover, with $K^0 = K^\infty + \sum_{I=1}^{N_v} K_I^e$, the quantity $P^{e0} = K^0 u$ is the total elastic force at the outset of deformation. It is noted that the elastic force P^{e0} can be derived from a pure mechanical potential function of the form $U^{\text{Mech}} = \frac{1}{2} K^0 u^2$, namely $P^{e0} = \mathrm{d}U^{\text{Mech}}/\mathrm{d}u$.

The evolution equation for the damper displacement α_I is obtained by equating the action and reaction force between the spring and damper in the I'th viscoelastic branch, namely $\eta \dot{\alpha}_I = K_I^e(u - \alpha_I)$. By multiplying both sides of this relation by K_I^e it follows that the evolution equation in terms of Q_I is given by

$$\dot{Q}_I + \frac{1}{\tau_I} Q = \frac{K_I^e}{\tau_I} u = \frac{g_I}{\tau_I} P^{e0}, \quad g_I = \frac{K_I^e}{K^0} \geq 0, \quad \tau_I = \frac{\eta_I}{K_I^e}. \tag{9}$$

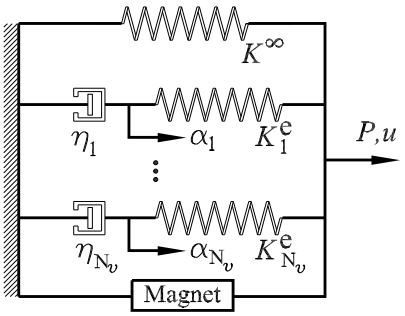

Fig. 2. One dimensional rheological model of the viscoelastic formulation.

Here, τ_I is the relaxation time of the I'th branch. By assuming zero forces and displacements as $t \to -\infty$, the exact solution for Q_I furnishes

$$\begin{aligned} Q_I(t) &= \frac{g_I}{\tau_I} \int_{-\infty}^{t} \exp\Big(\frac{\xi - t}{\tau_I}\Big) P^{e0}(\xi)\mathrm{d}\xi \\ &= g_I \Big(P^{e0}(\xi) - \int_{-\infty}^{t} \exp\Big(\frac{\xi - t}{\tau_I}\Big) \frac{\mathrm{d}}{\mathrm{d}\xi} P^{e0}(\xi)\mathrm{d}\xi \Big), \end{aligned} \tag{10}$$

where use has been made of integration by parts in the last equality. By substituting Eq. (10) into (8) it follows that the total force reads

$$\begin{aligned} &P = P^{\text{Mag}} + \int_{-\infty}^{t} g(t - \xi) \frac{\mathrm{d}}{\mathrm{d}\xi} P^{e0}(\xi)\mathrm{d}\xi \quad \text{with} \\ &g(t) = g_\infty + \sum_{I=1}^{N_v} g_I \exp\Big(\frac{-t}{\tau_I}\Big). \end{aligned} \tag{11}$$

Here, $g_\infty = K^\infty/K^0$, and $g(t)$ is the often referred to as the relaxation function. Clearly, the relation $g_\infty + \sum_{I=1}^{N_v} g_I = 1$ holds.

Before generalizing the rheological model to HMSMs, it is noted that the deformation gradient $\mathbf{F}^*$ can be multiplicatively decomposed into the dilatational part $\mathbf{F}_V^*$ and the isochoric one $\bar{\mathbf{F}}^*$ as follows (e.g., [57]):

$$\mathbf{F}^* = \mathbf{F}_V^* \bar{\mathbf{F}}^* \quad \text{with} \quad \bar{\mathbf{F}}^* = J^{*-\frac{1}{3}} \mathbf{F}^*, \quad \text{and} \quad \mathbf{F}_V^* = \mathbf{F}^* \bar{\mathbf{F}}^{*-1}, \tag{12}$$

where $J^* = \det \mathbf{F}^*$. From Eq. (12), straightforward calculations leads to the following relations:

$$\begin{aligned} &\frac{\partial \bar{\mathbf{F}}^*}{\partial \mathbf{F}^*} = J^{*-\frac{1}{3}} \boldsymbol{\mathcal{Z}}^{*\text{Dev}} \quad \text{with} \quad \boldsymbol{\mathcal{Z}}^{*\text{Dev}} = \boldsymbol{\mathcal{I}}^* - \frac{1}{3} \mathbf{F}^{*-\top} \otimes \mathbf{F}^* \quad \text{or} \\ &\mathcal{Z}_{ijpq}^{*\text{Dev}} = \mathcal{I}_{ijpq}^* - \frac{1}{3} F_{ij}^{*-\top} F_{pq}^*. \end{aligned} \tag{13}$$

Here, $\boldsymbol{\mathcal{I}}^*$ is a fourth-order tensor whose components are $\mathcal{I}_{ijpq}^* = \delta_{ip}^* \delta_{jq}^*$, and δ_{ip}^* is the three-dimensional Kronecker delta. Motivated by the expression for $\boldsymbol{\mathcal{Z}}^{*\text{Dev}}$, it is possible to define the fourth-order tensor $\boldsymbol{\mathcal{Z}}^{*\text{Vol}}$, and the deviatoric and volumetric parts of a two-point second-order tensor $\mathbf{T}^*$ as follows:

$$\left.\begin{aligned} &\boldsymbol{\mathcal{Z}}^{*\text{Vol}} = \boldsymbol{\mathcal{I}}^* - \boldsymbol{\mathcal{Z}}^{*\text{Dev}} = \frac{1}{3} \mathbf{F}^{*-\top} \otimes \mathbf{F}^*, \\ &\mathbf{T}^{*\text{Dev}} = \boldsymbol{\mathcal{Z}}^{*\text{Dev}} : \mathbf{T}^* = \mathbf{T}^* - \frac{1}{3} (\mathbf{T}^* : \mathbf{F}^*) \mathbf{F}^{*-\top} \\ &\mathbf{T}^{*\text{Vol}} = \boldsymbol{\mathcal{Z}}^{*\text{Vol}} : \mathbf{T}^* = \frac{1}{3} (\mathbf{T}^* : \mathbf{F}^*) \mathbf{F}^{*-\top}, \\ &\mathbf{T}^{*\text{Dev}} + \mathbf{T}^{*\text{Vol}} = \boldsymbol{\mathcal{I}}^* : \mathbf{T}^* = \mathbf{T}^* \end{aligned}\right\}. \tag{14}$$

Moreover, the relations $(\mathbf{T}^{*\text{Vol}})^{\text{Dev}} = \boldsymbol{\mathcal{Z}}^{*\text{Dev}} : \mathbf{T}^{*\text{Vol}} = \mathbf{0}$ and $(\mathbf{T}^{*\text{Dev}})^{\text{Vol}} = \boldsymbol{\mathcal{Z}}^{*\text{Vol}} : \mathbf{T}^{*\text{Dev}} = \mathbf{0}$ are valid. The relations expressed in Eqs. (13) and (14) play central roles in the present viscoelastic formulation.

Now, the free energy per unit reference volume of an HMSM as the summation of the mechanical and magnetic contributions is considered, namely [26]

$$\Psi = \Psi^{\text{Mech}} + \Psi^{\text{Mag}}, \quad \Psi^{\text{Mech}}(\mathbf{F}^*) = \Theta(J^*) + \Psi^{\text{Dev}}(\bar{\mathbf{F}}^*), \tag{15}$$

where the mechanical contribution Ψ^{Mech} is expressed as the summation of the volumetric part $\Theta(J^*)$ and the deviatoric one $\Psi^{\text{Dev}}(\bar{\mathbf{F}}^*)$. Following Zhao et al. [26], the magnetic part of the free energy density is considered to be

$$\Psi^{\text{Mag}} = -\frac{1}{\mu_0}\mathbf{F}^*\tilde{\mathbb{B}}^{*\text{r}} \cdot \mathbb{B}^{*\text{ext}}, \tag{16}$$

where $\mu_0 = 4\pi \times 10^{-7}\,\frac{N}{A^2}$ is the magnetic permeability of the free space. From Eqs. (15) and (16), the instantaneous first Piola–Kirchhoff stress $\mathbf{P}^{*\text{ins}}$ reads

$$\mathbf{P}^{*\text{ins}} = \frac{\partial \Psi}{\partial \mathbf{F}^*} = \mathbf{P}^{*\text{Mech}} + \mathbf{P}^{*\text{Mag}} \quad \text{with} \quad \mathbf{P}^{*\text{Mech}} = \mathbf{P}^{*\text{Vol}} + \mathbf{P}^{*\text{Dev}}. \tag{17}$$

Here, $\mathbf{P}^{*\text{Vol}}$, $\mathbf{P}^{*\text{Dev}}$, and $\mathbf{P}^{*\text{Mag}}$ are, respectively, the volumetric, deviatoric, and magnetic part of the stress, and are given by

$$\left.\begin{aligned} \mathbf{P}^{*\text{Vol}} = \frac{\partial \Theta}{\partial \mathbf{F}^*} = f_1(J^*)\mathbf{F}^{*-\top}, \quad \mathbf{P}^{*\text{Dev}} = \frac{\partial \Psi^{\text{Dev}}}{\partial \mathbf{F}^*} = J^{*-\frac{1}{3}}\bar{\mathbf{P}}^{*\text{Dev}} \\ \mathbf{P}^{*\text{Mag}} = \frac{\partial \Psi^{\text{Mag}}}{\partial \mathbf{F}^*} = -\frac{1}{\mu_0}\mathbb{B}^{*\text{ext}} \otimes \tilde{\mathbb{B}}^{*\text{r}} \end{aligned}\right\}, \tag{18}$$

where $f_1(J^*) = J^*\mathrm{d}\Theta/\mathrm{d}J^*$ and $\bar{\mathbf{P}}^* = \partial\Psi^{\text{Dev}}(\bar{\mathbf{F}}^*)/\partial\bar{\mathbf{F}}^*$. Obviously, the relations $\mathbf{P}^{*\text{Dev}} = \mathcal{Z}^{*\text{Dev}} : \mathbf{P}^{*\text{Mech}}$ and $\mathbf{P}^{*\text{Vol}} = \mathcal{Z}^{*\text{Vol}} : \mathbf{P}^{*\text{Mech}}$ hold. Additionally, as a consequence of the form of the magnetic part of free energy density, Ψ^{Mag}, the magnetic part of the stress, $\mathbf{P}^{*\text{Mag}}$, is independent of X_2.

Next, the continuum body is assumed to be stress-free as $t \to -\infty$. Motivated by the expression for the total force in Eq. (11), the term P^{e0} must be replaced by $\mathbf{P}^{*\text{Mech}}$. On the other hand, based on experimental observations only the deviatoric part of stress contributes to the convolution integral (e.g., Simo [56]). Consequently, from Eq. (11), the expression for the viscoelastic first Piola–Kirchhoff stress takes the form

$$\begin{aligned} \mathbf{P}^* &= \mathbf{P}^{*\text{Mag}} + \mathbf{P}^{*\text{Vol}} + \int_{-\infty}^{t} g(t-\xi)\frac{\partial}{\partial \xi}\mathbf{P}^{*\text{Dev}}(\mathbb{X},\xi)\mathrm{d}\xi \\ &= \mathbf{P}^{*\text{Mag}} + \mathbf{P}^{*\text{Vol}} + g_\infty \mathbf{P}^{*\text{Dev}} + \sum_{I=1}^{N_v} g_I \mathbf{Y}_I^*(\mathbb{X},t), \end{aligned} \tag{19}$$

where the second-order tensor $\mathbf{Y}_I^*(\mathbb{X},t)$ is defined by

$$\mathbf{Y}_I^*(\mathbb{X},t) = \int_{-\infty}^{t} \exp\left(\frac{\xi - t}{\tau_I}\right)\frac{\partial}{\partial \xi}\mathbf{P}^{*\text{Dev}}(\mathbb{X},\xi)\mathrm{d}\xi. \tag{20}$$

Following straightforward manipulations (e.g., [56,58]), a recursive formula for $\mathbf{Y}_I^*(\mathbb{X},t)$ at the discrete time $t = t_{n+1}$ is given by

$$\begin{aligned} \mathbf{Y}_I^*(\mathbb{X},t_{n+1}) = \exp\left(\frac{-\Delta t}{2\tau_I}\right)\left[\mathbf{P}^{*\text{Dev}}(\mathbb{X},t_{n+1}) - \mathbf{P}^{*\text{Dev}}(\mathbb{X},t_n)\right] \\ + \exp\left(\frac{-\Delta t}{\tau_I}\right)\mathbf{Y}_I^*(\mathbb{X},t_n), \end{aligned} \tag{21}$$

where $\Delta t = t_{n+1} - t_n$ is the time increment. Now, by substituting Eq. (21) into (19) the expression for the stress $\mathbf{P}^*(\mathbb{X},t)$ at $t = t_{n+1}$ is obtained. Moreover, the consistent fourth-order tensor $\mathcal{A}^*$ is obtained by differentiating the viscoelastic stress $\mathbf{P}^*$ with respect to the deformation gradient $\mathbf{F}^*$ at the time t_{n+1}. Accordingly, from Eqs. (19) and (21) it follows that

$$\mathcal{A}^* = \left.\frac{\partial \mathbf{P}^*}{\partial \mathbf{F}^*}\right|_{t_{n+1}} = \mathcal{A}^{*\text{Vol}} + \tilde{g}(\Delta t)\mathcal{A}^{*\text{Dev}}, \tag{22}$$

The expressions for the fourth-order tensors $\mathcal{A}^{*\text{Vol}} = (\partial\mathbf{P}^{*\text{Vol}}/\partial\mathbf{F}^*)_{t_{n+1}}$ and $\mathcal{A}^{*\text{Dev}} = (\partial\mathbf{P}^{*\text{Dev}}/\partial\mathbf{F}^*)_{t_{n+1}}$, and the algorithmic relaxation function $\tilde{g}(\Delta t)$ are given by

$$\mathcal{A}^{*\text{Vol}} = f_2(J^*)\mathbf{F}^{*-\top} \otimes \mathbf{F}^{*-\top} - f_1(J^*)\mathbf{F}^{*-\top} \boxtimes \mathbf{F}^{*-\top}, \tag{23}$$

$$\begin{aligned} \mathcal{A}^{*\text{Dev}} = \frac{1}{3}\Big\{ & J^{*-\frac{1}{3}}[(\mathbf{F}^* : \bar{\mathbf{P}}^*)\mathbf{F}^{*-\top} \boxtimes \mathbf{F}^{*-\top} - \mathbf{F}^{*-\top} : \bar{\mathbf{P}}^*] - \mathbf{P}^{*\text{Dev}} \otimes \mathbf{F}^{*-\top} \\ & + J^{*-\frac{2}{3}}[(\mathbf{F}^* \boxtimes \mathbf{F}^*) :: \bar{\mathcal{A}}^*\mathbf{F}^{*-\top} \otimes \mathbf{F}^{*-\top} \\ & - (\mathbf{F}^{*-\top} \boxtimes \mathbf{F}^*) : \bar{\mathcal{A}}^* + 3\bar{\mathcal{A}}^* : \mathcal{P}^{*\text{Dev}}] \Big\}, \end{aligned} \tag{24}$$

$$\tilde{g}(\Delta t) = g_\infty + \sum_{I=1}^{N} g_I \exp\left(\frac{-\Delta t}{2\tau_I}\right), \tag{25}$$

where $f_2(J^*) = f_1(J^*) + J^{*2}\mathrm{d}^2\Theta/\mathrm{d}J^{*2}$ and $\bar{\mathcal{A}}^* = \partial\bar{\mathbf{P}}^*/\partial\bar{\mathbf{F}}^* = \partial^2\Psi^{\text{Dev}}/\partial\bar{\mathbf{F}}^*\partial\bar{\mathbf{F}}^*$. It is noted that in deriving Eqs. (23) and (24) use has been made of the relation $\partial\mathbf{F}^{*-\top}/\partial\mathbf{F}^* = -\mathbf{F}^{*-\top} \boxtimes \mathbf{F}^{*-\top}$.

The three-dimensional viscoelasticity formulated in this subsection is specialized to planar HMS beams in the next subsection.

3.2. Viscoelasticity formulation for HMS beams

Hard-magnetic soft materials are considered to be incompressible or quasi-incompressible in the literature (e.g., [26]). For the case of beams deforming in the X_1X_2 plane, it is possible to enforce the plane stress condition and the incompressibility constraint simultaneously. To do so, it is noted that the deformation gradient tensor $\mathbf{F}$ in Eq. (3) is the two-dimensional version of the tensor $\mathbf{F}^*$ in 3-space, given by

$$\mathbf{F}^* = \mathbf{F} + \lambda_3 \mathbf{e}_3 \otimes \mathbf{e}_3, \quad J^* = \det\mathbf{F}^* = \lambda_3 \det\mathbf{F} = \lambda_3 J. \tag{26}$$

where λ_3 is the stretch in the X_3 direction. The incompressibility of HMSMs leads to

$$J^* = 1, \quad \lambda_3 = J^{-1}. \tag{27}$$

On the other hand, for the case of isotropic materials, the mechanical part of the free energy may be written as (e.g., [57])

$$\Psi^{\text{Mech}}(\mathbf{F}^*) = \Psi^{\text{Dev}}(I_1^*, I_2^*) - p(J^* - 1), \tag{28}$$

where $I_1^* = \mathrm{tr}\mathbf{C}^*$ and $I_2^* = \frac{1}{2}(I_1^{*2} - \mathrm{tr}\mathbf{C}^{*2})$ are the first two invariants of the three dimensional right Cauchy–Green deformation $\mathbf{C}^* = \mathbf{F}^{*\top}\mathbf{F}^*$, and p is a Lagrange multiplier, which is often referred to as the hydrostatic pressure. By differentiating the latter equation with respect to $\mathbf{F}^*$, the mechanical part of the stress tensor is calculated. After adding the magnetic part of stress, it is possible to calculate the hydrostatic pressure p via the plane stress condition. As an example, for the case of *incompressible neo-Hookean* materials, the mechanical part of strain energy density is given by $\Psi^{\text{Dev}}(I_1^*, I_2^*) = \frac{1}{2}\mu(I_1^* - 3)$. Accordingly, the instantaneous first Piola–Kirchhoff stress takes the form

$$\mathbf{P}^{*\text{ins}} = \mathbf{P}^{*\text{Dev}} + \mathbf{P}^{*\text{Vol}} + \mathbf{P}^{\text{Mag}} \quad \text{with} \quad \mathbf{P}^{*\text{Dev}} = \mu\mathbf{F}^* \quad \text{and} \quad \mathbf{P}^{*\text{Vol}} = -p\mathbf{F}^{*-\top}. \tag{29}$$

Moreover, $\mathbf{P}^{\text{Mag}} = -\frac{1}{\mu_0}\mathbb{B}^{\text{ext}} \otimes \tilde{\mathbb{B}}^{\text{r}}$ is the magnetic part of the stress in the X_1X_2 plane. It is noted that in the present formulation, since $\mathbb{B}^{\text{ext}}$ and $\tilde{\mathbb{B}}^{\text{r}}$ lie in the X_1X_2 plane, the magnetic stress $\mathbf{P}^{\text{Mag}}$ does not contribute in the X_3 direction.

For the case of pure elastic deformations, the plane stress condition $\mathbf{P}_{33}^{*\text{ins}} = 0$ results in the following expression for the hydrostatic pressure p, and the volumetric and deviatoric parts

of the stress in the X_1X_2 plane:

$$p = \mu\lambda_3^2 = \mu J^{-2}, \quad \mathbf{P}^{\text{Vol}} = -\mu J^{-2}\mathbf{F}^{-\top}, \quad \mathbf{P}^{\text{Dev}} = \mu\mathbf{F}. \tag{30}$$

However, for the case of viscoelastic deformations, the hydrostatic pressure p at the time $t = t_{n+1}$ can be found by enforcing the plane stress condition $P^*_{33} = 0$ in Eq. (19). Accordingly, using Eqs. (21) and (27), and after a lengthy but straightforward manipulations, the hydrostatic pressure p may be written as

$$p(\mathbb{X}, t_{n+1}) = \alpha_1 J^{-2} + \alpha_2(J^{-2} - J^{-1}J^{-1(n)}) + \alpha_3 J^{-1}, \tag{31}$$

where the superscript $^{(n)}$ denotes the underlying quantity at the time $t = t_n$. Moreover, the quantities denoted by α_S $(S = 1, 2, 3)$ are defined by

$$\begin{aligned} &\alpha_1 = \mu g_\infty, \quad \alpha_2 = \mu \sum_{I=1}^{N_v} g_I \exp\left(\frac{-\Delta t}{2\tau_I}\right), \\ &\alpha_3 = \sum_{I=1}^{N_v} g_I Y^{*(n)}_{I33} \exp\left(\frac{-\Delta t}{\tau_I}\right), \end{aligned} \tag{32}$$

where $Y^{*(n)}_{I33}$ is the 33 component of the tensors $\mathbf{Y}^*_I$ at the time t_n. Now, the expressions for the fourth-order tensors $\boldsymbol{\mathcal{A}}^{\text{Vol}}$ and $\boldsymbol{\mathcal{A}}^{\text{Dev}}$ in the two-dimensional space take the form

$$\boldsymbol{\mathcal{A}}^{\text{Vol}} = q\mathbf{F}^{-\top}\otimes\mathbf{F}^{-\top} + p\mathbf{F}^{-\top}\boxtimes\mathbf{F}^{-\top}, \quad \boldsymbol{\mathcal{A}}^{\text{Dev}} = \mu\boldsymbol{\mathcal{I}}. \tag{33}$$

Here, $\boldsymbol{\mathcal{I}}$ is the two-dimensional version of the fourth-order tensor $\boldsymbol{\mathcal{I}}^*$ defined after Eq. (13). Moreover, the function q in Eq. $(33)_1$ is given by

$$q = -\frac{\partial p}{\partial J} = 2\alpha_1 J^{-2} + \alpha_2(2J^{-2} - J^{-1}J^{-1(n)}) + \alpha_3 J^{-1}. \tag{34}$$

Based on Eqs. (3), (5), (6), (18)–(24), and (31)–(34), it is possible to approximate any generic member Φ in the set $\mathcal{S} = \{\alpha_3, p, q, \mathbf{P}^{\text{Vol}}, \mathbf{P}^{\text{Dev}}, \boldsymbol{\mathcal{A}}\}$ in the following form:

$$\Phi \approx \Phi^{(0)} + X_2\Phi^{(1)} \quad \text{for} \quad \Phi \in \mathcal{S}. \tag{35}$$

In particular, from $\mathbf{P}^{\text{Dev}} \approx \mathbf{P}^{\text{Dev}(0)} + X_2\mathbf{P}^{\text{Dev}(1)}$ and Eq. (20), the approximation $\mathbf{Y}_I \approx \mathbf{Y}^{(0)}_I + X_2\mathbf{Y}^{(1)}_I$ $(I = 1, 2, \ldots, N_v)$ is deduced. This allows one to write $\alpha_3 \approx \alpha_3^{(0)} + X_2\alpha_3^{(1)}$. Similarly, approximations for $\mathbf{P}^{\text{Vol}}$, $\mathbf{P}^{\text{Dev}}$, and $\mathbf{Y}_I$, beside the expression of the magnetic stress $\mathbf{P}^{\text{Mag}}$, leads to the relation $\mathbf{P} \approx \mathbf{P}^{(0)} + X_2\mathbf{P}^{(1)}$ for the planar viscoelastic first Piola–Kirchhoff stress tensor. In particular, for the *incompressible neo-Hookean* materials one obtains

$$\left.\begin{aligned} p^{(0)} &= \alpha_1\hat{J}^{(0)} + \alpha_2(\hat{J}^{(0)} - \tilde{J}^{(0)}\tilde{J}^{(0)(n)}) + \alpha_3^{(0)}\tilde{J}^{(0)} \\ p^{(1)} &= \alpha_1\hat{J}^{(1)} + \alpha_2(\hat{J}^{(1)} - \tilde{J}^{(0)}\tilde{J}^{(1)(n)} - \tilde{J}^{(1)}\tilde{J}^{(0)(n)}) + \alpha_3^{(1)}\tilde{J}^{(0)} + \alpha_3^{(0)}\tilde{J}^{(1)} \end{aligned}\right\}, \tag{36}$$

$$\left.\begin{aligned} q^{(0)} &= 2\alpha_1\hat{J}^{(0)} + \alpha_2(2\hat{J}^{(0)} - \tilde{J}^{(0)}\tilde{J}^{(0)(n)}) + \alpha_3^{(0)}\tilde{J}^{(0)} \\ q^{(1)} &= 2\alpha_1\hat{J}^{(1)} + \alpha_2(2\hat{J}^{(1)} - \tilde{J}^{(0)}\tilde{J}^{(1)(n)} - \tilde{J}^{(1)}\tilde{J}^{(0)(n)}) + \alpha_3^{(1)}\tilde{J}^{(0)} + \alpha_3^{(0)}\tilde{J}^{(1)} \end{aligned}\right\}, \tag{37}$$

$$\mathbf{P}^{\text{Dev}(0)} = \mu\mathbf{F}^{(0)}, \quad \mathbf{P}^{\text{Dev}(1)} = \mu\mathbf{F}^{(1)}, \tag{38}$$

$$\mathbf{P}^{\text{Vol}(0)} = -p^{(0)}\tilde{\mathbf{F}}^{(0)}, \quad \mathbf{P}^{\text{Vol}(1)} = -(p^{(0)}\tilde{\mathbf{F}}^{(1)} + p^{(1)}\tilde{\mathbf{F}}^{(0)}), \tag{39}$$

$$\boldsymbol{\mathcal{A}}^{(0)} = \mu\tilde{g}\boldsymbol{\mathcal{I}} + q^{(0)}\tilde{\mathbf{F}}^{(0)}\otimes\tilde{\mathbf{F}}^{(0)} + p^{(0)}\tilde{\mathbf{F}}^{(0)}\boxtimes\tilde{\mathbf{F}}^{(0)}, \tag{40}$$

$$\begin{aligned} \boldsymbol{\mathcal{A}}^{(1)} =& q^{(0)}(\tilde{\mathbf{F}}^{(0)}\otimes\tilde{\mathbf{F}}^{(1)} + \tilde{\mathbf{F}}^{(1)}\otimes\tilde{\mathbf{F}}^{(0)}) + p^{(0)}(\tilde{\mathbf{F}}^{(0)}\boxtimes\tilde{\mathbf{F}}^{(1)} + \tilde{\mathbf{F}}^{(1)}\boxtimes\tilde{\mathbf{F}}^{(0)}) \\ &+ q^{(1)}\tilde{\mathbf{F}}^{(0)}\otimes\tilde{\mathbf{F}}^{(0)} + p^{(1)}\tilde{\mathbf{F}}^{(0)}\boxtimes\tilde{\mathbf{F}}^{(0)}, \end{aligned} \tag{41}$$

where use has been made of Eq. (22). The consistent tangent tensor $\boldsymbol{\mathcal{A}}$ and its expression of the form $\boldsymbol{\mathcal{A}} \approx \boldsymbol{\mathcal{A}}^{(0)} + X_2\boldsymbol{\mathcal{A}}^{(1)}$ will be used in the next section for constructing the material part of the element stiffness matrix in the FE formulation.

Remark. It is worthwhile to mention that by setting $g_I = 0$ $(I = 1, 2, \ldots, N_v)$, or equivalently $g_\infty = 1$, in the formulation developed above, the non-equilibrium viscoelastic effects disappear and the formulation for magneto-hyperelastic HMS beams is retrieved.

4. FE formulation

In this section, a finite element formulation for the numerical analysis of viscoelastic HMS beams in the Lagrangian framework is developed. The deformation is time-dependent and quasi-static so that the inertia effects are neglected.

The main tool for developing the formulation is the virtual work principle, namely $\delta\mathcal{U} = \delta\mathcal{W}$ [55]. Here, $\delta\mathcal{U}$ and $\delta\mathcal{W}$ are the virtual internal energy and the virtual work of external loads, respectively. To start the formulation, the beam in the reference configuration is discretized into N_E elements, and a typical element $\Omega^{\mathcal{E}}$ is considered. It is assumed that the element contains N_N nodes with u_1, u_2, and ψ as its degrees of freedom. The field variables $\{u_1, u_2, \psi\}$ are interpolated as follows:

$$\{u_1, u_2, \psi\} = \sum_{I=1}^{N_N} N_I\{U_I, V_I, \Psi_I\}, \tag{42}$$

where N_I is the I'th shape function and that $\{U_I, V_I, \Psi_I\}$ are the nodal values of the fields $\{u_1, u_2, \psi\}$ at the I'th node. The virtual internal energy of the typical element, denoted by $\delta\mathcal{U}^{\mathcal{E}}$, may be written as

$$\delta\mathcal{U}^{\mathcal{E}} = \int_{V_{\Omega\mathcal{E}}} \mathbf{P}:\delta\mathbf{F}\mathrm{d}V = \int_{L_{\Omega\mathcal{E}}} \sum_{S=1}^{3} \delta\mathbb{E}^{(S)\top}\mathbb{P}^{(S)}\mathrm{d}X_1, \tag{43}$$

where $V_{\Omega\mathcal{E}}$ and $L_{\Omega\mathcal{E}}$ are the volume and length of the typical element. Moreover, the vector-like quantities $\mathbb{E}^{(S)}$ and $\mathbb{P}^{(S)}$ $(S = 1, 2, 3)$ are defined by

$$\mathbb{E}^{(1)} = \begin{Bmatrix} 1 + u_1' \\ \cos\psi \end{Bmatrix}, \quad \mathbb{E}^{(2)} = \begin{Bmatrix} -\sin\psi \\ u_2' \end{Bmatrix}, \quad \mathbb{E}^{(3)} = \begin{Bmatrix} -\psi'\cos\psi \\ -\psi'\sin\psi \end{Bmatrix}, \tag{44}$$

$$\mathbb{P}^{(1)} = \tilde{A}\begin{Bmatrix} P^{(0)}_{11} \\ P^{(0)}_{22} \end{Bmatrix}, \quad \mathbb{P}^{(2)} = \tilde{A}\begin{Bmatrix} P^{(0)}_{12} \\ P^{(0)}_{21} \end{Bmatrix}, \quad \mathbb{P}^{(3)} = \tilde{I}\begin{Bmatrix} P^{(1)}_{11} \\ P^{(1)}_{21} \end{Bmatrix}, \tag{45}$$

where $\tilde{A}$ and $\tilde{I}$ are the cross-sectional area and the moment of inertia of the beam cross-section about the X_3-axis, respectively. Using Eqs. (42) and (44), the expressions for $\delta\mathbb{E}^{(S)}$ $(S = 1, 2, 3)$ may be written in the following discretized form:

$$\delta\mathbb{E}^{(S)} = \sum_{I=1}^{N_N} \mathbb{B}^{(S)}_I\delta\mathbb{U}_I. \tag{46}$$

Here, $\delta\mathbb{U}_I = \{\delta U_I, \delta V_I, \delta\Psi_I\}^\top$ represents the virtual generalized displacement of the I'th node. Additionally, the 2×3 matrices $\mathbb{B}^{(S)}_I$ $(S = 1, 2, 3)$ have the following nonzero components:

$$\left.\begin{aligned} &(\mathbb{B}^{(1)}_I)_{11} = N_I', \quad (\mathbb{B}^{(1)}_I)_{23} = -N_I\sin\psi, \\ &(\mathbb{B}^{(2)}_I)_{13} = -N_I\cos\psi, \quad (\mathbb{B}^{(2)}_I)_{22} = N_I' \\ &(\mathbb{B}^{(3)}_I)_{13} = N_I\psi'\sin\psi - N_I'\cos\psi, \\ &(\mathbb{B}^{(3)}_I)_{23} = -N_I\psi'\cos\psi - N_I'\sin\psi \end{aligned}\right\}. \tag{47}$$

By substituting Eq. (46) into (43) it follows that the discretized form of $\delta\mathcal{U}^{\mathcal{E}}$ may be written as

$$\delta\mathcal{U}^{\mathcal{E}} = \sum_{I=1}^{N_N} \delta\mathbb{U}_I^{\top}\mathbb{F}_I^{\text{int}} \quad \text{with} \quad \mathbb{F}_I^{\text{int}} = \sum_{S=1}^{3}\int_{L_{\Omega^{\mathcal{E}}}} \delta\mathbb{B}^{(S)\top}\mathbb{P}^{(S)}\mathrm{d}X_1. \tag{48}$$

Here, $\mathbb{F}_I^{\text{int}}$ is the internal force vector on the I'th node. Next, the virtual external work $\delta\mathcal{W}^{\mathcal{E}}$ on the typical element may be written as

$$\begin{aligned}\delta\mathcal{W}^{\mathcal{E}} = &\int_{L_e}(\tilde{q}_1\delta u_1 + \tilde{q}_2\delta u_2 + \tilde{q}_3\delta\psi)\mathrm{d}X_1 \\ &+ \sum_{I=1}^{N_N}(\tilde{Q}_{1I}\delta U_I + \tilde{Q}_{2I}\delta V_I + \tilde{Q}_{3I}\delta\Psi_I),\end{aligned} \tag{49}$$

where $\tilde{q}_1$ denotes the force per unit length in X_1 direction, $\tilde{q}_2$ is the force per unit length in X_2 direction and $\tilde{q}_3$ presents the bending moment per unit length around X_3-axis. Also, $\tilde{Q}_{1I}$ stands for the point force in X_1 direction, $\tilde{Q}_{2I}$ represents the point force in X_2 direction, and $\tilde{Q}_{3I}$ designates the concentrated bending moment around the X_3-axis acting on the I'th node of the typical element. Using Eq. (42), adopted for the virtual field variables, it is possible to express $\delta\mathcal{W}^{\mathcal{E}}$ in the following form:

$$\delta\mathcal{W}^{\mathcal{E}} = \sum_{I=1}^{N_N}\delta\mathbb{U}_I^{\top}\mathbb{F}_I^{\text{ext}} \quad \text{with} \quad \mathbb{F}_I^{\text{ext}} = \tilde{\mathbb{Q}}_I + \int_{L_{\Omega^{\mathcal{E}}}} N_I\tilde{\mathfrak{q}}\mathrm{d}X_1. \tag{50}$$

Here, $\mathbb{F}_I^{\text{ext}}$ represents the external force vector acting on the I'th node. Moreover, the definitions $\tilde{\mathfrak{q}} = \{\tilde{q}_1, \tilde{q}_2, \tilde{q}_3\}^{\top}$ and $\tilde{\mathbb{Q}}_I = \{\tilde{Q}_{1I}, \tilde{Q}_{2I}, \tilde{Q}_{3I}\}^{\top}$ have been used. Substituting Eqs. (48) and (50) into the virtual work principle, the system of nonlinear algebraic equations $\mathbb{R} = \mathbb{F}^{\text{int}} - \mathbb{F}^{\text{ext}} = \mathbf{0}$ is obtained. Here, $\mathbb{F}^{\text{int}}$ and $\mathbb{F}^{\text{ext}}$ are, respectively, the assembled internal and external force vectors, and $\mathbb{R}$ is the assembled residual vector of the typical element. To solve the system of equations via the Newton–Raphson method, it is essential to obtain the linearized form of the equations. Accordingly, the increment of the virtual internal energy of the typical element furnishes

$$\begin{aligned}\Delta\delta\mathcal{U}^{\mathcal{E}} &= \int_{V_{\Omega^{\mathcal{E}}}} \delta\mathbf{F}:\Delta\mathbf{P}\mathrm{d}V + \int_{V_{\Omega^{\mathcal{E}}}} \Delta\delta\mathbf{F}:\mathbf{P}\mathrm{d}V \\ &= \int_{V_{\Omega^{\mathcal{E}}}} \delta\mathbf{F}:\boldsymbol{\mathcal{A}}:\Delta\mathbf{F}\mathrm{d}V + \int_{L_{\Omega^{\mathcal{E}}}}\sum_{S=1}^{3}\Delta\delta\mathbb{E}^{(S)\top}\mathbb{P}^{(S)}\mathrm{d}X_1.\end{aligned} \tag{51}$$

Employing Eqs. (3) and (35), the first integrand in Eq. (51) may be written as

$$\begin{aligned}\delta\mathbf{F}:\boldsymbol{\mathcal{A}}:\Delta\mathbf{F} = &\ \delta\mathbf{F}^{(0)}:\boldsymbol{\mathcal{A}}^{(0)}:\Delta\mathbf{F}^{(0)} \\ &+ X_2[\delta\mathbf{F}^{(0)}:(\boldsymbol{\mathcal{A}}^{(0)}:\Delta\mathbf{F}^{(1)} + \boldsymbol{\mathcal{A}}^{(1)}:\Delta\mathbf{F}^{(0)}) + \delta\mathbf{F}^{(1)}:\boldsymbol{\mathcal{A}}^{(0)}:\Delta\mathbf{F}^{(0)}] \\ &+ X_2^2[\delta\mathbf{F}^{(0)}:\boldsymbol{\mathcal{A}}^{(1)}:\Delta\mathbf{F}^{(0)} + \delta\mathbf{F}^{(1)}:(\boldsymbol{\mathcal{A}}^{(0)}:\Delta\mathbf{F}^{(1)} + \boldsymbol{\mathcal{A}}^{(1)}:\Delta\mathbf{F}^{(0)})].\end{aligned} \tag{52}$$

Converting this equation into matrix form and integrating over the cross-sectional area of the element leads to the following expression for the third integral in Eq. (51):

$$\int_{V_{\Omega^{\mathcal{E}}}} \delta\mathbf{F}:\boldsymbol{\mathcal{A}}:\Delta\mathbf{F}\mathrm{d}V = \sum_{I=1}^{N_N}\sum_{J=1}^{N_N}\delta\mathbb{U}_I^{\top}\mathbb{K}_{IJ}^{\text{mat}}\Delta\mathbb{U}_J, \tag{53}$$

where $\mathbb{K}_{IJ}^{\text{mat}}$ is the IJ'th block of the material stiffness matrix as follows:

$$\begin{aligned}\mathbb{K}_{IJ}^{\text{mat}} = &\int_{L_{\Omega^{\mathcal{E}}}} \mathbb{B}_I^{(1)}[\tilde{A}(\mathbb{A}^{(1)}\mathbb{B}_J^{(1)} + \mathbb{A}^{(2)}\mathbb{B}_J^{(2)}) + \tilde{I}\mathbb{A}^{(3)}\mathbb{B}_J^{(3)}]\mathrm{d}X_1 \\ &+ \int_{L_{\Omega^{\mathcal{E}}}} \tilde{I}\mathbb{B}_I^{(3)}(\mathbb{A}^{(4)}\mathbb{B}_J^{(1)} + \mathbb{A}^{(5)}\mathbb{B}_J^{(2)} + \mathbb{A}^{(6)}\mathbb{B}_J^{(3)})\mathrm{d}X_1 \\ &+ \int_{L_{\Omega^{\mathcal{E}}}} \mathbb{B}_I^{(2)}[\tilde{A}(\mathbb{A}^{(7)}\mathbb{B}_J^{(1)} + \mathbb{A}^{(8)}\mathbb{B}_J^{(2)}) + \tilde{I}\mathbb{A}^{(9)}\mathbb{B}_J^{(3)}]\mathrm{d}X_1.\end{aligned} \tag{54}$$

Here, the 2×2 matrices $\mathbb{A}^{(S)}$ $(S = 1, 2, \ldots, 9)$ are given by

$$\left.\begin{aligned}&\mathbb{A}^{(1)} = \begin{bmatrix}\mathcal{A}^{(0)}_{1111} & \mathcal{A}^{(0)}_{1122}\\ \mathcal{A}^{(0)}_{2211} & \mathcal{A}^{(0)}_{2222}\end{bmatrix},\ \mathbb{A}^{(2)} = \begin{bmatrix}\mathcal{A}^{(0)}_{1112} & \mathcal{A}^{(0)}_{1121}\\ \mathcal{A}^{(0)}_{2212} & \mathcal{A}^{(0)}_{2221}\end{bmatrix},\\ &\mathbb{A}^{(3)} = \begin{bmatrix}\mathcal{A}^{(1)}_{1111} & \mathcal{A}^{(1)}_{1121}\\ \mathcal{A}^{(1)}_{2211} & \mathcal{A}^{(1)}_{2221}\end{bmatrix}\\ &\mathbb{A}^{(4)} = \begin{bmatrix}\mathcal{A}^{(1)}_{1111} & \mathcal{A}^{(1)}_{1122}\\ \mathcal{A}^{(1)}_{2111} & \mathcal{A}^{(1)}_{2122}\end{bmatrix},\ \mathbb{A}^{(5)} = \begin{bmatrix}\mathcal{A}^{(1)}_{1112} & \mathcal{A}^{(1)}_{1121}\\ \mathcal{A}^{(1)}_{2112} & \mathcal{A}^{(1)}_{2121}\end{bmatrix},\\ &\mathbb{A}^{(6)} = \begin{bmatrix}\mathcal{A}^{(0)}_{1111} & \mathcal{A}^{(0)}_{1121}\\ \mathcal{A}^{(0)}_{2111} & \mathcal{A}^{(0)}_{2121}\end{bmatrix}\\ &\mathbb{A}^{(7)} = \begin{bmatrix}\mathcal{A}^{(0)}_{1211} & \mathcal{A}^{(0)}_{1222}\\ \mathcal{A}^{(0)}_{2111} & \mathcal{A}^{(0)}_{2122}\end{bmatrix},\ \mathbb{A}^{(8)} = \begin{bmatrix}\mathcal{A}^{(0)}_{1212} & \mathcal{A}^{(0)}_{1221}\\ \mathcal{A}^{(0)}_{2211} & \mathcal{A}^{(0)}_{2221}\end{bmatrix},\\ &\mathbb{A}^{(9)} = \begin{bmatrix}\mathcal{A}^{(1)}_{1211} & \mathcal{A}^{(1)}_{1221}\\ \mathcal{A}^{(1)}_{2111} & \mathcal{A}^{(1)}_{2121}\end{bmatrix}\end{aligned}\right\}. \tag{55}$$

On the other hand, the latest integral in Eq. (51) leads to

$$\int_{L_{\Omega^{\mathcal{E}}}}\sum_{S=1}^{3}\Delta\delta\mathbb{E}^{(S)\top}\mathbb{P}^{(S)}\mathrm{d}X_1 = \sum_{I=1}^{N_N}\sum_{J=1}^{N_N}\delta\mathbb{U}_I^{\top}\mathbb{K}_{IJ}^{\text{geo}}\Delta\mathbb{U}_J, \tag{56}$$

where $\mathbb{K}_{IJ}^{\text{geo}}$ is the IJ'th block of the geometric stiffness matrix, given by

$$\mathbb{K}_{IJ}^{\text{geo}} = \mathbb{M}\int_{L_{\Omega^{\mathcal{E}}}}(\beta_1 + \beta_2 + \beta_3)\mathrm{d}X_1. \tag{57}$$

Here, $\mathbb{M}$ is a 3×3 matrix the only nonzero component of which is $M_{33} = 1$. Moreover, the scalar functions β_I $(I = 1, 2, 3)$ are as follows:

$$\left.\begin{aligned}\beta_1 &= -P_2^{(1)}\cos\psi N_I N_J,\\ \beta_2 &= P_1^{(2)}\sin\psi N_I N_J\\ \beta_3 &= (P_1^{(3)}\sin\psi - P_2^{(3)}\cos\psi)(N_I' N_J + N_I N_J')\\ &\quad + (P_1^{(3)}\cos\psi + P_2^{(3)}\sin\psi)N_I N_J\end{aligned}\right\}, \tag{58}$$

where $P_I^{(S)}$ $(S = 1, 2, 3,\ I = 1, 2)$ is the I'th component of $\mathbb{P}^{(S)}$ defined in Eq. (45). Accordingly, the IJ'th block of the element stiffness matrix becomes $\mathbb{K}_{IJ}^{\mathcal{E}} = \mathbb{K}_{IJ}^{\text{mat}} + \mathbb{K}_{IJ}^{\text{geo}}$. Finally, after performing the assembly procedure, a linear algebraic equation of the form $\mathbb{K}\Delta\tilde{\mathfrak{u}} = -\mathbb{R}$ is obtained, which is solved for the incremental assembled generalized displacement vector $\Delta\tilde{\mathfrak{u}}$.

5. Numerical examples

In this section, to examine the performance of the present formulation, several numerical examples are solved. To do so, a home-written FE code based on the formulation developed in the previous sections has been provided. In all simulations, beam elements with three nodes, and three DOFs $\{u_1, u_2, \psi\}$ at each node, are employed. Additionally, the quasi-static shear modulus is considered to be $\mu = 303$ kPa, and the material is assumed to be fully incompressible. Furthermore, all beams under consideration have constant rectangular cross-sections, and the width of all cross-sections is 5 mm.

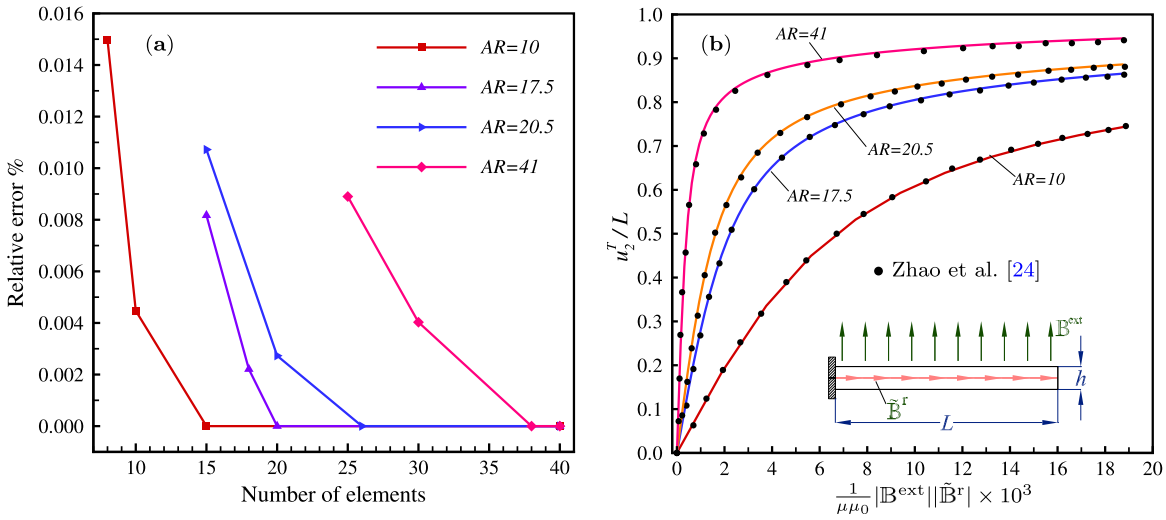

Fig. 3. Convergence of the lateral deflection vs. the number of elements (**a**), the nondimensional tip deflection u_2^T/L versus the nondimensional load parameter $\frac{1}{\mu\mu_0}|\mathbb{B}^{ext}||\tilde{\mathbb{B}}^r| \times 10^3$ (**b**).

Table 1
Beam dimensions, number of elements and load steps, and the maximum lateral deflection under the applied magnetic induction $\mathbb{B}^{ext} = 50\mathbb{e}_2$ (mT)

L (mm)	h (mm)	$AR = \frac{L}{h}$	$N_{Elements}$	$N_{Load\ steps}$	u^T_{2conv} (mm)
11	1.1	10	15	10	8.1782
19.2	1.1	≈ 17.5	20	10	16.6101
17.2	0.84	≈ 20.5	26	20	15.2407
17.2	0.42	≈ 41	38	30	16.2617

5.1. Elastic bending of cantilever beams under a magnetic loading with $\varphi = \pi/2$

In this example, finite elastic bending of cantilever beams under an external magnetic flux perpendicular to the undeformed beams is investigated. This example has been previously studied numerically and experimentally in [26,44]. Here, it is shown that the present formulation can generate the results previously reported in the literature.

Four cantilever beams with the dimensions indicated in Table 1 are considered. The aspect ratio "*AR*" is defined as the ratio of the length L over the thickness h of the beams. The referential residual magnetic flux density is considered to be $\tilde{\mathbb{B}}^r = 0.143\ \mathbb{e}_1$ (T). The beams are subjected to the external magnetic flux density of the form $\mathbb{B}^{ext} = |\mathbb{B}^{ext}|\mathbb{e}_2$. In other words, the angle φ in Fig. 1 is considered to be $\pi/2$. The value of $|\mathbb{B}^{ext}|$ varies gradually from 0 to $|\mathbb{B}^{ext}_{max}| = 50$ mT for the four beams.

Convergence of the maximum lateral deflection versus the number of elements is displayed in Fig. 3(**a**). The relative error is defined as $|u_2^T - u^T_{2conv}| \times 100/u^T_{2conv}$. Here, u_2^T is the lateral deflection at the beam tip, and u^T_{2conv} is the converged value. Accordingly, the minimum number of elements and the converged values of lateral deflections are provided in the table.

Variation of the nondimensional tip deflection u_2^T/L against the nondimensional load parameter $\frac{1}{\mu\mu_0}|\mathbb{B}^{ext}||\tilde{\mathbb{B}}^r| \times 10^3$ is demonstrated in Fig. 3(**b**). It is observed that the results based on the present formulation are almost coincident with those obtained in [26]. The deformed shapes of the beams at ten load steps, when the magnitude of the applied flux density is of the form $|\mathbb{B}^{ext}| = \frac{S}{10}|\mathbb{B}^{ext}_{max}|$ ($S = 1, 2, \ldots, 10$), are illustrated in Fig. 4(**a**–**d**). It is noted that the slender beam with $AR = 41$ exhibits very large deformations even for small values of the applied flux density. For example, as is observed from Fig. 4(**d**), under $|\mathbb{B}^{ext}| = 5$ mT, the lateral deflection in this beam is about $0.8L$.

5.2. Elastic bending of cantilever beams under an anti-parallel magnetic loading ($\varphi = \pi$)

In this example, finite elastic bending of two cantilever beams under an external magnetic loading of the form $\mathbb{B}^{ext} = -|\mathbb{B}^{ext}|\mathbb{e}_1$ (namely $\varphi = \pi$) is investigated. The cantilever beams under study are those with the aspect ratios $AR = 20.5$ and $AR = 41$ whose geometric data have been already provided in Table 1. Once more, the referential residual magnetic flux density is given by $\tilde{\mathbb{B}}^r = 0.143\ \mathbb{e}_1$ (T). The magnitude of the magnetic loading, $|\mathbb{B}^{ext}|$, varies gradually from 0 to 40 mT. Deformation of the beam with $AR = 20.5$ has been modeled numerically and experimentally by Zhao et al. [26].

Convergence of the lateral tip deflection versus the number of elements is depicted in Fig. 5(**a**). It is observed that the minimum number of elements in the beams with $AR = 20.5$ and $AR = 41$ is $N_E = 35$ and $N_E = 40$, respectively. The number of load steps in both simulations is $N_{LS} = 80$. Moreover, for the mentioned beams, the final value of the lateral tip deflection is obtained to be 7.8952 and 3.9550 (mm), respectively.

As shown in Fig. 5(**a**), the angle between the tangent line to the tip of the deformed beam and the X_1-axis is denoted by θ. The nondimensional tip deflection u_2^T/L and the normalized angle θ/π versus the nondimensional loading parameter $\frac{1}{\mu\mu_0}|\mathbb{B}^{ext}||\tilde{\mathbb{B}}^r| \times 10^3$ are displayed in Fig. 5(**b**). It is observed that the results of the present formulation for the beam with $AR = 20.5$ are in good agreement with those obtained by Zhao et al. [26]. The deformed shapes of the beams at 40 load steps, when the magnitude of the applied flux density is of the form $|\mathbb{B}^{ext}| = \frac{S}{40}|\mathbb{B}^{ext}_{max}|$ ($S = 1, 2, \ldots, 40$), is illustrated in Fig. 6.

5.3. Viscoelastic deformation of a HMS cantilever beam with constant $\tilde{\mathbb{B}}^r$

In this example, the time-dependent response of the HMS cantilever beam with $AR = 20.5$, considered in the previous examples, is investigated. Similar to the previous two examples, the constant referential residual magnetic flux density $\tilde{\mathbb{B}}^r = 0.143\ \mathbb{e}_1$ (mT) is considered along the beam. To model the viscous effects, a viscoelastic branch in addition to the pure elastic one

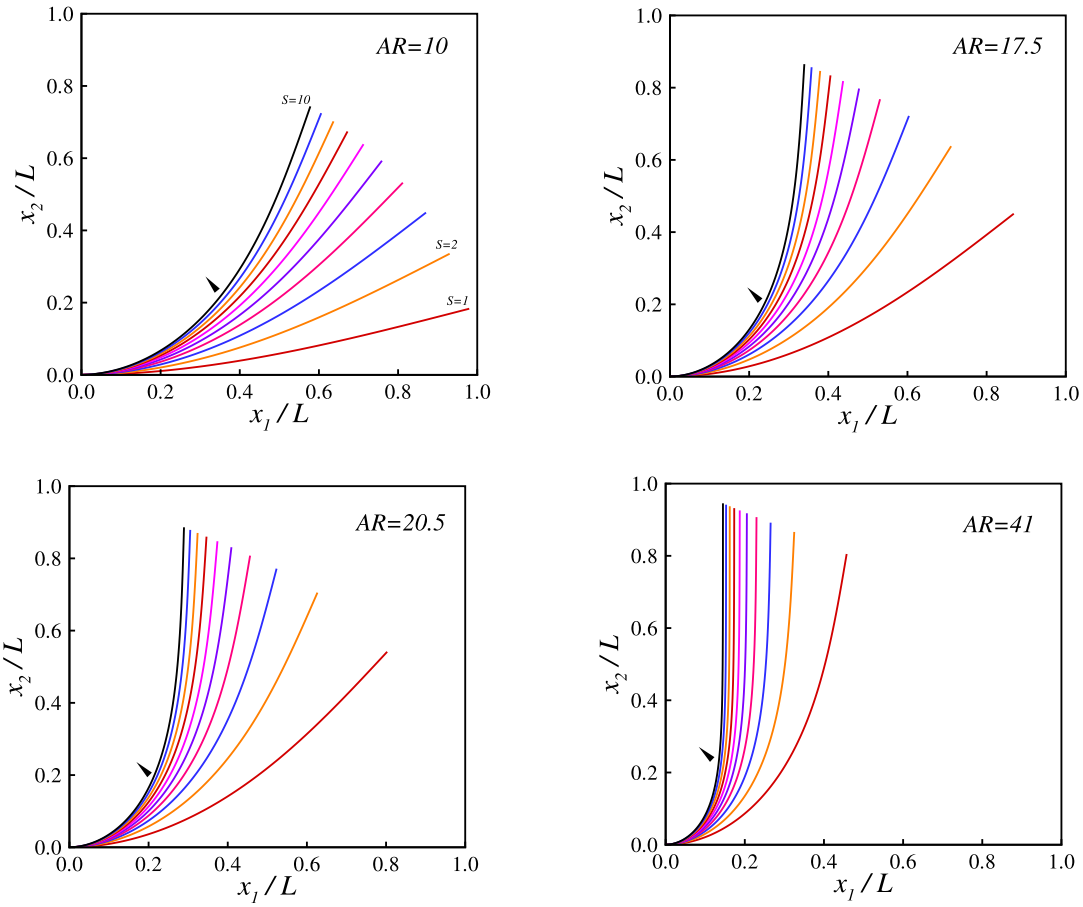

Fig. 4. Deformed shapes of the cantilever beams under $\mathbb{B}^{\text{ext}} = |\mathbb{B}^{\text{ext}}|e_1$ corresponding to $|\mathbb{B}^{\text{ext}}| = 5S$ (mT, $S = 1, 2, \ldots, 10$).

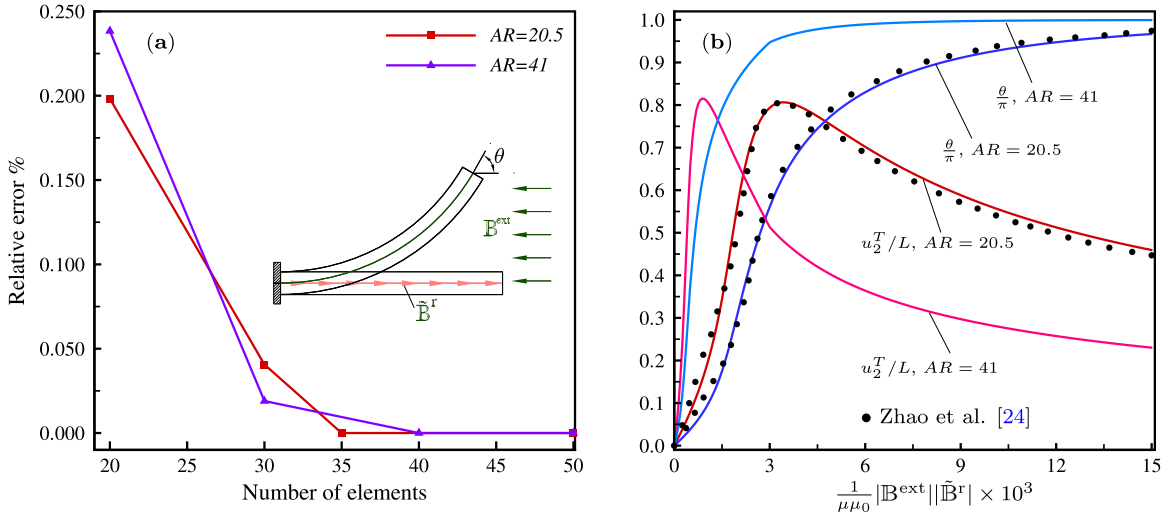

Fig. 5. Convergence of the lateral deflection vs. the number of elements (**a**), the nondimensional tip deflection u_2^{T}/L and the normalized angle θ/π vs. the nondimensional load parameter $\frac{1}{\mu\mu_0}|\mathbb{B}^{\text{ext}}||\tilde{\mathbb{B}}^{\text{r}}| \times 10^3$ (**b**).

is considered. The external magnetic loading of the form $\mathbb{B}^{\text{ext}} = |\mathbb{B}^{\text{ext}}|e_2$ is applied to the beam. The magnitude of the magnetic loading, $|\mathbb{B}^{\text{ext}}|$, varies linearly from 0 to 50 (mT) in 2 seconds. It is then held fixed to observe the creep response of the HMS beam. In all simulations, the time increment for the loading stage is $\Delta t = 0.1$ s and that of the creeping stage is $\Delta t = 0.5$ s.

Two different cases are considered. In the first case, the relaxation time is considered to be $\tau = 5$ s and the deformation is simulated for $t_{\text{max}} = 10$ seconds. Therefore, in this case, the total number of load steps is 36. Convergence of the lateral tip deflection versus the number of elements, for several values of the nondimensional long term shear modulus g_∞, is displayed in Fig. 7(**a**). It is noted that the case $g_\infty = 1$ models the pure elastic deformation of the beam. From the figure, it is observed that the minimum number of elements to model all cases is $N_E = 30$. Next, three material points T_I ($I = 1, 2, 3$) located at the position

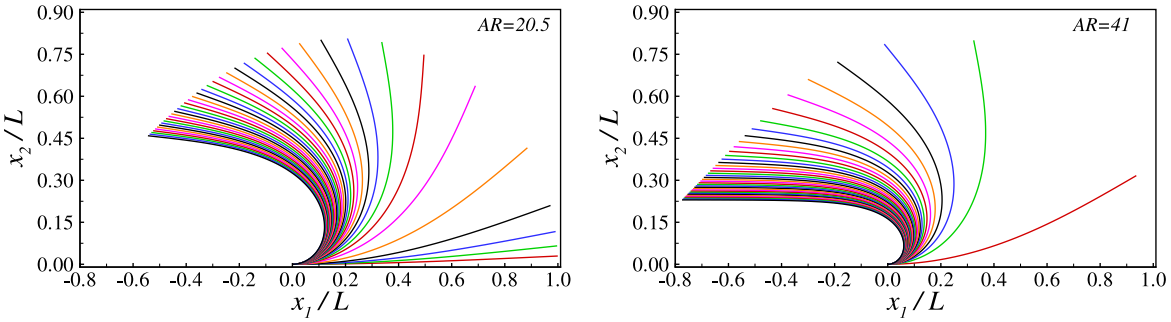

Fig. 6. Deformed shapes of the cantilever beams with $AR = 20.5$ and $AR = 41$ under $\mathbb{B}^{\text{ext}} = -|\mathbb{B}^{\text{ext}}|\mathbb{e}_1$ corresponding to $|\mathbb{B}^{\text{ext}}| = S$ (mT, $S = 1, 2, \ldots, 40$).

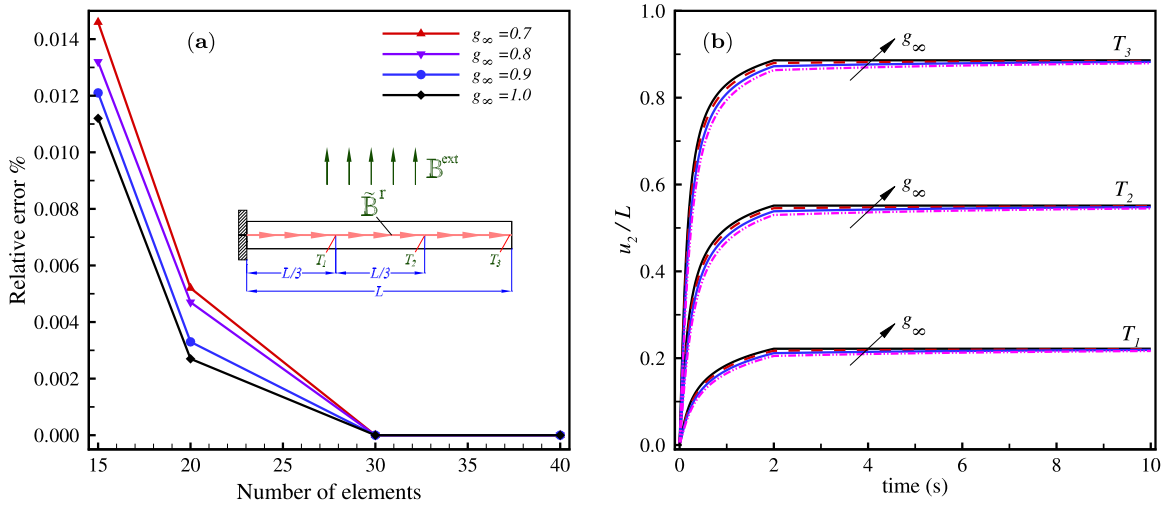

Fig. 7. Convergence of the lateral deflection vs the number of elements (**a**), time history of the lateral deflection at the points T_I ($I = 1, 2, 3$) for $\tau = 5$ s and various values of $g_\infty \in \{0.7, 0.8, 0.9, 1.0\}$ (**b**).

$X_{1I} = \frac{1}{3}IL$ on the beam centerline are considered. Time history of the nondimensional lateral deflection u_2/L at the material points T_I, for different values of $g_\infty \in \{0.7, 0.8, 0.9, 1.0\}$, is depicted in Fig. 7(**b**). As can be seen from the figure, for small values of g_∞, which are equivalent to larger viscous effects, the lateral deflection is smaller than that of pure elastic deformation. This indicates that the viscous branch increases the resistance of the material to deformation, which is a well-known phenomenon in viscoelastic deformations (e.g., [59–61]). On the other hand, it is observed that for large values of time, viscoelastic effects vanish and the results based on all values of g_∞ converge to that of the pure elastic deformation corresponding to $g_\infty = 1$.

For the second case of simulations, it is assumed that $g_\infty = 0.7$, and the deformation is modeled for several values of the relaxation time τ. To observe the difference between the curves, the maximum time is considered to be $t_{\max} = 4$ seconds. Time history of the nondimensional lateral deflection u_2/L at the material points T_I ($I = 1, 2, 3$), for different values of τ, is demonstrated in Fig. 8(**a**). From the figure, it is observed that the viscous effects are larger for larger values of the relaxation time τ. This means that for small values of τ, viscoelastic effects vanish rapidly. In contrast, more time is needed to diminish the viscous effects if the relaxation is a large value, which is a widely-observed experimental phenomenon of typical viscoelastic polymers, see [62].

Finally, the deformed shapes of the beam, for $g_\infty = 0.7$, $\tau = 5$ s, and at several load steps are illustrated in Fig. 8(**b**). For the loading stage with $t \in [0, 2]$ s, the 11 curves corresponding to $t = 0.1$ s and $t = 0.2S$ ($S = 1, 2, \ldots, 10$) are displayed in the figure. Moreover, for the creeping stage, the curves corresponding to $t = 5$ and $t = 10$ s are included in the figure. Based on the above-mentioned explanations, the deformed shape corresponding to $t = 10$ s is approximately equivalent to the final deformed shape of the beam in pure elastic deformation as displayed in Fig. 4(**c**).

5.4. Viscoelastic deformation of an HMS cantilever beam with variable $\tilde{\mathbb{B}}^r$ along the beam

In this example, the time-dependent response of an HMS cantilever with variable residual magnetic flux is studied. The length and height of the beam are considered to be $L = 18$ and $h = 0.5$ (mm), respectively. For the referential residual magnetic flux density, shown in Fig. 9(**a**), it is assumed that $\tilde{\mathbb{B}}^{\text{r}} = 0.143\ \mathbb{e}_1$ (mT) for $X_1 \in [0, \frac{1}{3}L) \cup (\frac{2}{3}L, L]$, and $\tilde{\mathbb{B}}^{\text{r}} = -0.143\ \mathbb{e}_1$ (mT) for $X_1 \in [\frac{1}{3}L, \frac{2}{3}L]$. It is noted that this is an idealized assumption. From the practical point of view, there has to be a small gap between magnetic poles of the same name, which is assumed to be zero in the present work.

The maximum applied magnetic flux density, loading history, relaxation times, and loading cases are exactly the same as those explained in the previous example.

For the first case of loading, the convergence of the lateral tip deflection versus the number of elements is depicted in Fig. 9(**a**). Accordingly, to capture the beam deformation for various values of the nondimensional long term shear modulus g_∞, the minimum required number of elements is $N_E = 45$. Time history of the nondimensional lateral deflection u_2/L at the material points

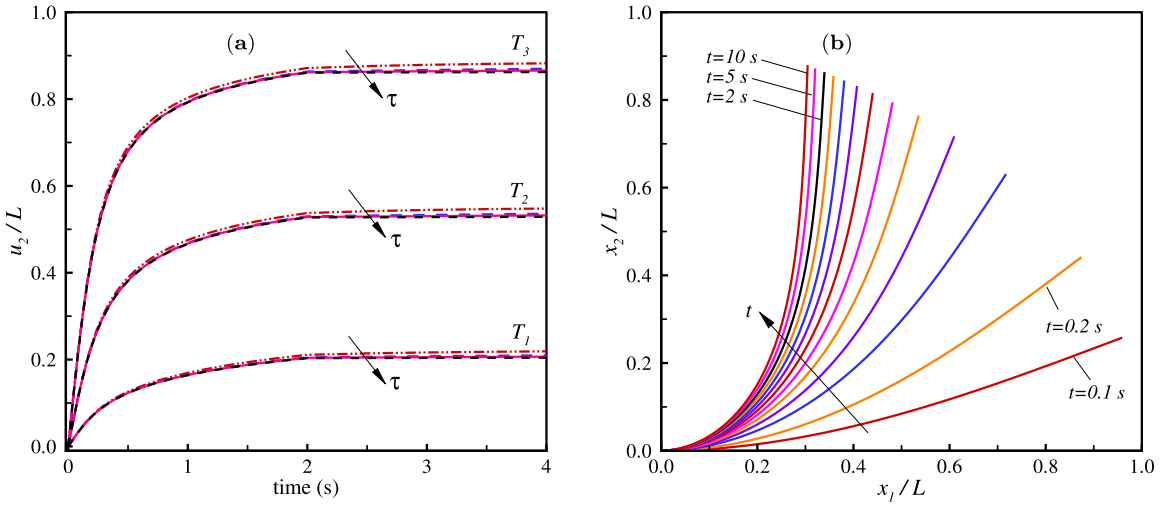

Fig. 8. Time history of the lateral deflection at the material points T_I ($I = 1, 2, 3$) for $g_\infty = 0.7$ and various values of $\tau \in \{1, 5, 10, 30\}$ s (**a**), deformed shapes of the beam at different times $t \in \{0.1, 0.2S, 5, 10\}$ s, ($S = 1, 2, \ldots, 10$, $g_\infty = 0.7$, $\tau = 5$ s) (**b**).

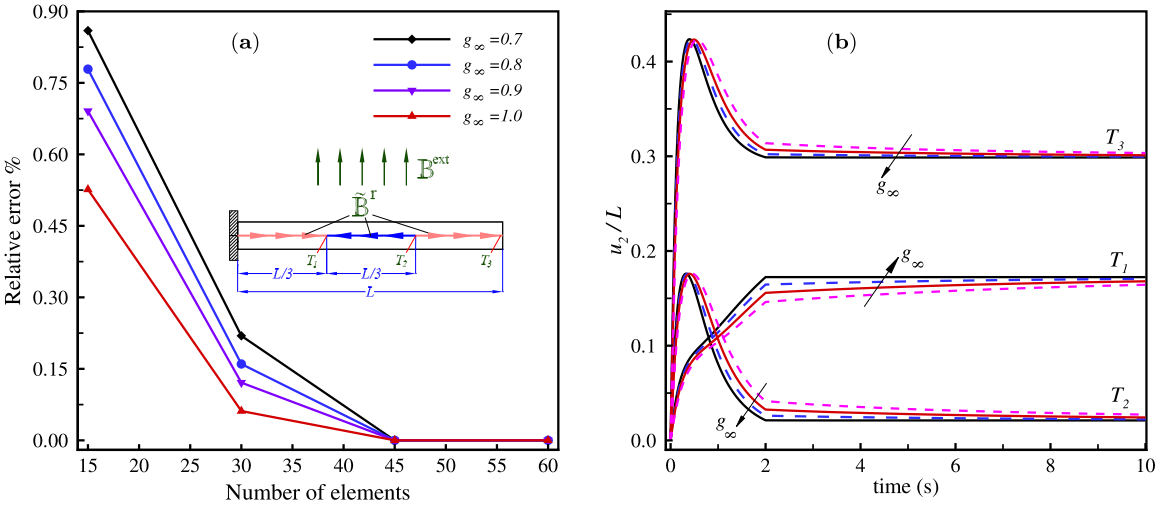

Fig. 9. Convergence of the lateral deflection vs the number of elements (**a**), time history of the lateral deflection at the points T_I ($I = 1, 2, 3$) for $\tau = 5$ s and various values of $g_\infty \in \{0.7, 0.8, 0.9, 1.0\}$ (**b**).

T_I ($I = 1, 2, 3$), for several values of g_∞, is displayed in Fig. 9(**b**). In this specific example, the lateral deflection u_2 of the material point T_1, initially located at $X_1 = \frac{1}{3}L$, is an ever-increasing function of time. For this point, the magnitude of u_2 increases by increasing the value of g_∞. Once more, it is observed that the lateral deflection decreases by increasing the viscoelastic effects. For large values of the time t, all curves coincide with that of the pure elastic deformation corresponding to $g_\infty = 1$.

Next, by considering $g_\infty = 0.7$, deformation of the beam under various values of the relaxation time τ is studied. Variation of the nondimensional lateral deflection u_2/L vs time at the material points T_I ($I = 1, 2, 3$) is depicted in Fig. 10(**a**). From the curves corresponding to the material point T_1, it is concluded that the viscous effects are larger for larger values of the relaxation time τ.

The deformed shapes of the beam, for $g_\infty = 0.7$ and $\tau = 5$ s, and for various values of time, are demonstrated in Fig. 10(**b**). More precisely, the curves in the figure correspond to $t = 0.1$, $t = 0.2S$ ($S = 1, 2, \ldots, 10$), $t = 5$, and $t = 10$ s. Once more, the last curve that corresponds to $t = 10$ s is approximately coincident with the final deformed shape of the beam in a quasi-static pure elastic deformation.

5.5. Viscoelastic deformation of a clamped-simply supported HMS beam with variable $\tilde{\mathbb{B}}^r$

In this example, the viscoelastic response of an HMS beam clamped at one end and simply supported at the other end is studied. It is noted the simple support is free to move along the X_1 direction. The length, height, loading conditions, time increments, and loading cases are the same as those described in the previous example. However, the maximum value of the applied magnetic induction is $|\mathbb{B}^{ext}| = 100$ mT. Once more, to account for the viscous effects, a single viscoelastic branch is considered; and the referential residual magnetic flux density is considered to be variable along the beam length. As shown in Fig. 11(**a**), it is assumed that $\tilde{\mathbb{B}}^r = 0.143\ e_1$ (mT) for $X_1 \in [0, \frac{1}{4}L) \cup (\frac{3}{4}L, L]$, and $\tilde{\mathbb{B}}^r = -0.143\ e_1$ (mT) for $X_1 \in [\frac{1}{4}L, \frac{3}{4}L]$.

In the first case, the relaxation time is considered to be $\tau = 5$ s and by considering different values for $g_\infty \in \{0.7, 0.8, 0.9, 1.0\}$,

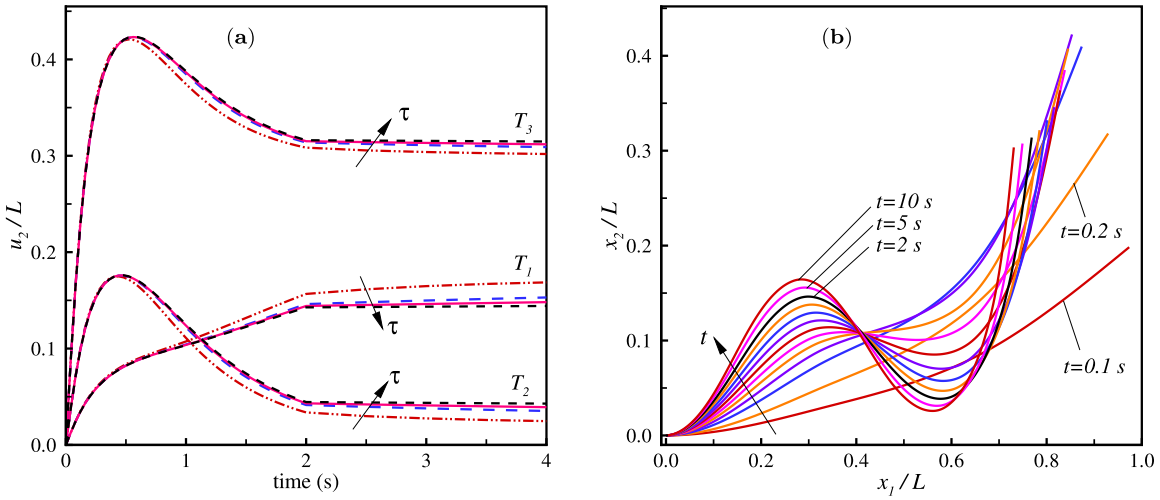

Fig. 10. Time history of the lateral deflection at the material points T_I ($I = 1, 2, 3$) for $g_\infty = 0.7$ and various values of $\tau \in \{1, 5, 10, 30\}$ s (**a**), deformed shapes of the beam at different times $t \in \{0.1, 0.2S, 5, 10\}$ s ($S = 1, 2, \ldots, 10$, $g_\infty = 0.7$, $\tau = 5$ s) (**b**).

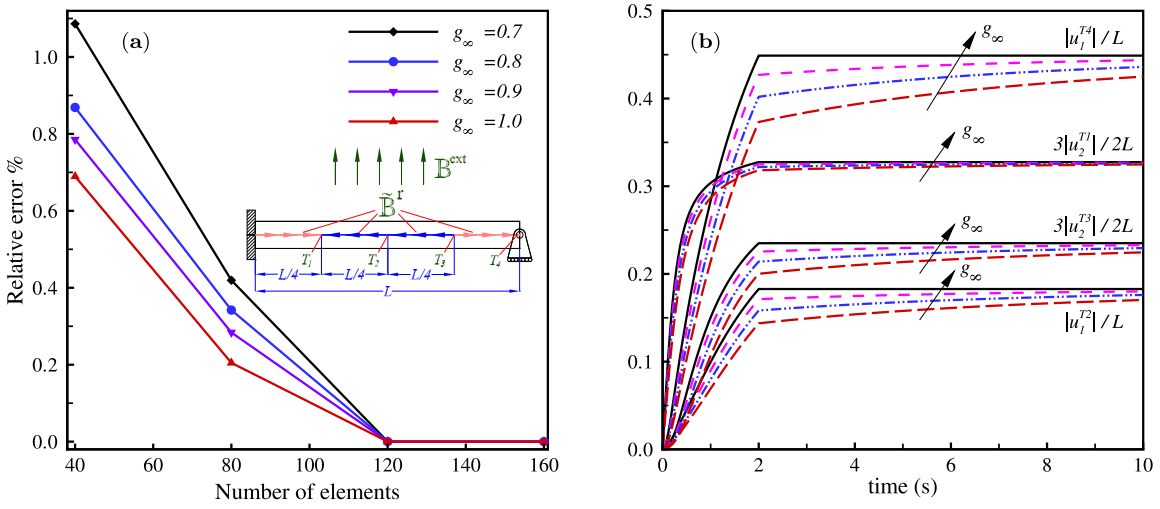

Fig. 11. Convergence of the lateral deflection vs the number of elements (**a**), time history of $\frac{3|u_2|}{2L}$ (at T_1 and T_3) and $\frac{|u_1|}{L}$ (at T_2 and T_4) for $\tau = 5$ s and various values of $g_\infty \in \{0.7, 0.8, 0.9, 1.0\}$ (**b**).

the deformation is simulated for $t_{\max} = 10$ seconds. From the convergence analysis of the lateral tip deflection, as shown in Fig. 11(**a**), it is observed that the minimum required number of elements is $N_E = 120$. Four material points T_I ($I = 1, 2, 3, 4$) located at the position $X_{1I} = \frac{1}{4}IL$ on the beam centerline are considered. Time histories of the nondimensional axial displacement $|u_1|/L$ (at the material points T_1 and T_4), and the nondimensional lateral displacement $3|u_2|/2L$ (at the material points T_2 and T_3) are demonstrated in Fig. 11(**b**). The coefficient 3/2 in $3|u_2|/2L$ is used to separate different curves from each other. Similar to the previous example, it is observed by reducing the value of g_∞, viscoelastic effects increase, and the resistance of the material to deformation increases. Obviously, for large values of time, all curves converge to the pure elastic solution characterized by $g_\infty = 1$.

For the second set of simulations, by considering the fixed value of $g_\infty = 0.7$, the deformation analysis is performed for different values of the relaxation time τ. Once more, the maximum time is considered to be $t_{\max} = 4$ seconds. Variation of the nondimensional axial displacement $|u_1|/L$ (at the material points T_1 and T_4), and the nondimensional lateral displacement $3|u_2|/2L$ (at the material points T_2 and T_3) versus time, and for different values of τ, is displayed in Fig. 12(**a**). The curves indicate that viscoelastic resistance increases by increasing the value of the relaxation time τ.

Next, the deformed shapes of the beam at various load steps are depicted in Fig. 12(**b**). The values of g_∞ and τ, and the times at which the deformations have been captured are the same as those mentioned in the previous two examples. It is observed that due to variable remnant magnetic flux along the beam, the deformed shape is very similar to a sinusoidal shape. Although, the magnitude of deflection at the material point T_3 is around 15% larger than that at the material point T_1.

6. Summary

In this work, a finite deformation framework for beams made of hard-magnetic soft materials by considering viscoelastic effects was formulated. As part of the formulation, a viscoelasticity formulation was developed that can be used for the analysis of 2D and 3D bodies, beams, plates, and shells made of HMSMs. After adopting the viscoelastic formulation for the case of beams, a

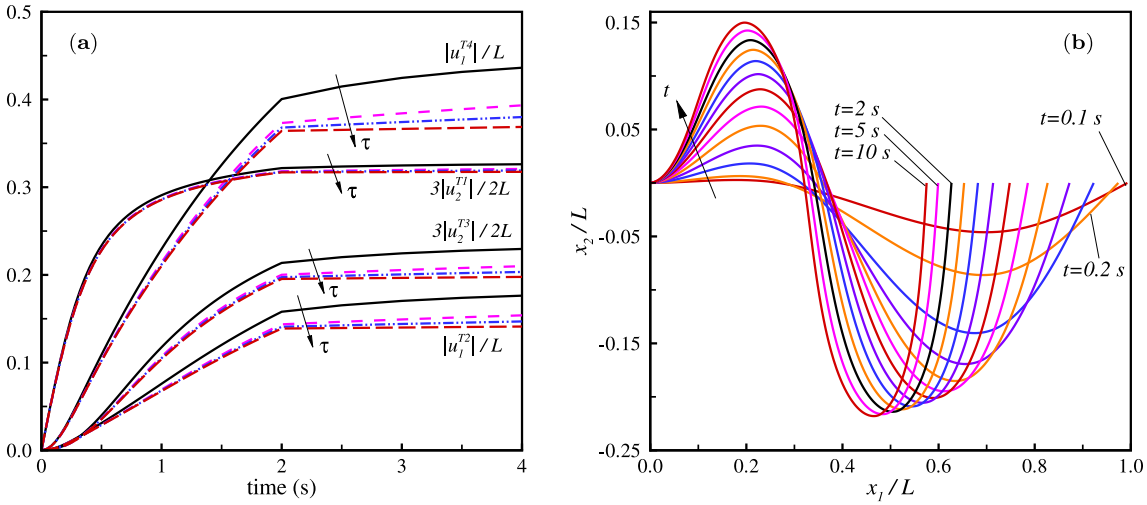

Fig. 12. Time history of $\frac{3|u_2|}{2L}$ (at T_1 and T_3) and $\frac{|u_1|}{L}$ (at T_2 and T_4) for $g_\infty = 0.7$ and various values of $\tau \in \{1, 5, 10, 30\}$ s (**a**), deformed shapes of the beam at different times $t \in \{0.1, 0.25, 5, 10\}$ s, $(S = 1, 2, \ldots, 10,\ g_\infty = 0.7,\ \tau = 5$ s) (**b**).

nonlinear finite element formulation for the numerical solution of problems was developed, and several numerical examples were solved. It was shown that for the case of purely elastic deformations, the present formulation can generate the results previously reported in the literature. For the case of viscoelastic deformations, the creep response of HMS beams was simulated, and the effects of viscoelastic parameters, e.g., relaxation time and the nondimensional long-term shear modulus were investigated. It was observed that the present formulation can model the pure elastic and viscoelastic deformation of HMS beams.

Declaration of competing interest

The authors declare that they have no known competing financial interests or personal relationships that could have appeared to influence the work reported in this paper.

Acknowledgments

M.H. acknowledges the funding through an Engineering and Physical Sciences Research Council (EPSRC) Impact Acceleration Award (EP/R511614/1).

References

[1] H. Böse, Viscoelastic properties of silicone-based magnetorheological elastomers, Int. J. Mod. Phys. B 21 (2007) 4790–4797.
[2] A. Boczkowska, S.F. Awietjan, Smart composites of urethane elastomers with carbonyl iron, J. Mater. Sci. 44 (2009) 4104–4111.
[3] I. Bica, The influence of the magnetic field on the elastic properties of anisotropic magnetorheological elastomers, J. Ind. Eng. Chem. 18 (2012) 1666–1669.
[4] G. Stano, G. Percoco, Additive manufacturing aimed to soft robots fabrication: A review, Extreme Mech. Lett. 42 (2021) 101079.
[5] D. Ivaneyko, V. Toshchevikov, M. Saphiannikova, G. Heinrich, Effects of particle distribution on mechanical properties of magneto-sensitive elastomers in a homogeneous magnetic field, Condens. Mat. Phys. 15 (2012) 33601.
[6] W. Hu, G. Zhan, M. Mastrangeli, M. Sitti, Small-scale soft-bodied robot with multimodal locomotion, Nature 554 (2018) 81–85.
[7] Y. Xia, J. Wang, R. Yang, T. Lu, T. Wang, Z. Suo, Untethered microbot powered by giant magnetoelastic strain, 2018, arXiv:1810.09060.
[8] Z. Ren, W. Hu, X. Dong, M. Sitti, Multi-functional soft-bodied jellyfish-like swimming, Nat. Commun. 10 (2019) 2703.
[9] A. Koivikko, D.-M. Drotlef, M. Sitti, V. Sariola, Magnetically switchable soft suction grippers, Extreme Mech. Lett. 44 (2021) 101263.
[10] M.A. Moreno-Mateos, J. Gonzalez-Rico, C. Gomez-Cruz, E. Nunez-Sardinha, M.L. Lopez-Donaire, S. Lucarini, A. Arias, A. Munoz-Barrutia, D. Velasco, D. Garcia-Gonzalez, Magneto-mechanical system to reproduce and quantify complex strain patterns in biological materials, Appl. Mat. Today 27 (2022) 101437.
[11] M. Schümann, D.Y. Borin, S. Huang, G.K. Auernhammer, R. Müller, S. Odenbach, A characterisation of the magnetically induced movement of NdFeB-particles in magnetorheological elastomers, Smart Mater. Struct. 26 (2017) 095018.
[12] K.A. Kalina, J. Brummund, P. Metsch, M. Kaestner, D.Y. Borin, J.M. Linke, S. Odenbach, Modeling of magnetic hystereses in soft MREs filled with NdFeB particles, Smart Mater. Struct. 26 (2017) 105019.
[13] Y. Kim, G.A. Parada, S. Liu, X. Zhao, Ferromagnetic soft continuum robots, Sci. Robot. 4 (2019) eaax7329.
[14] M. Eshaghi, M. Ghasemi, K. Khorshidi, Design, Manufacturing and applications of small-scale magnetic soft robots, Extreme Mech. Lett. 44 (2021) 101268.
[15] A. Dorfmann, R.W. Ogden, Nonlinear magnetoelastic deformations of elastomers, Acta Mech. 167 (2004) 13–28.
[16] K. Danas, S.V. Kankanala, N. Triantafyllidis, Experiments and modelling of iron-particled-filled magnetorheological elastomers, J. Mech. Phys. Solids 60 (2012) 120–138.
[17] P. Saxena, M. Hossain, P. Steinmann, A theory of finite deformation magneto-viscoelasticity, Int. J. Solids Struct. 50 (2013) 3886–3897.
[18] G. Ethiraj, C. Miehe, Multiplicative magneto-elasticity of magnetosensitive polymers incorporating micromechanically-based network kernels, Internat. J. Engrg. Sci. 102 (2016) 93–119.
[19] M. Mehnert, M. Hossain, P. Steinmann, Towards a thermo-magneto-mechanical coupling framework for magneto-rheological elastomers, Int. J. Solids Struct. 128 (2017) 117–132.
[20] R. Zabihyan, J. Mergheim, J.P. Pelteret, B. Brands, P. Steinmann, FE^2 simulations of magnetorheological elastomers: Influence of microscopic boundary conditions, microstructures and free space on the macroscopic responses of MREs, Int. J. Solids Struct. 193 (2020) 338–356.
[21] R. Bustamante, M.H.B.M. Shariff, M. Hossain, Mathematical formulations for elastic magneto-electrically coupled soft materials at finite strains: Time-independent processes, Int. J. Engrg. Sci. 159 (2021) 103429.
[22] M.A. Moreno-Mateos, M.L. Lopez-Donaire, M. Hossain, D. Garcia-Gonzalez, Effects of soft and hard magnetic particles on the mechanical performance of ultra-soft magnetorheological elastomers, Smart Mater. Struct. (2022) http://dx.doi.org/10.1088/1361-665X/ac6bd3.
[23] A.K. Bastola, M. Hossain, A review on magneto-mechanical characterizations of magnetorheological elastomers, Composites B 200 (2020) 108348.
[24] A.K. Bastola, M. Hossain, The shape-morphing performance of magnetoactive soft materials, Mater. Des. 211 (2021) 110172.
[25] S. Lucarini, M. Hossain, D. Garcia-Gonzalez, Recent advances in hard-magnetic soft composites: Synthesis, characterisation, computational modelling, and applications, Compos. Struct. 200 (2021) 210001.
[26] R. Zhao, Y. Kim, A.S. Chester, P. Sharma, X. Zhao, Mechanics of hard-magnetic soft materials, J. Mech. Phys. Solids 124 (2019) 244–263.
[27] P.A. Sanchez, O.V. Stolbov, S.S. Kantorovich, Y.L. Raikher, Modeling the magnetostriction effect in elastomers with magnetically soft and hard particles, Soft Matter 15 (2019) 7145.

[28] M. Schümann, D.Y. Borin, J. Morich, S. Odenbach, Reversible and non-reversible motion of NdFeB-particles in magnetorheological elastomers, J. Intell. Mater. Syst. Struct. 32 (2020) 3–15.
[29] M. Lee, T. Park, C. Kim, S.M. Park, Characterization of a magneto-active membrane actuator comprising hard magnetic particles with varying crosslinking degrees, Mater. Des. 195 (2020) 108921.
[30] G.Z. Lum, Z. Ye, X. Dong, H. Marvi, O. Erin, W. Hu, M. Sitti, Shape-programmable magnetic soft matter, Proc. Natl. Acad. Sci. 113 (2016) E6007–E6015.
[31] Y. Kim, H. Yuk, R. Zhao, S.A. Chester, X. Zhao, Printing ferromagnetic domains for untethered fast-transforming soft materials, Nature 558 (2018) 274–279.
[32] S. Wu, Q. Ze, R. Zhang, N. Hu, Y. Cheng, F. Yang, R. Zhao, Symmetry-breaking actuation mechanism for soft robotics and active metamaterials, ACS Appl. Mater. Interfaces 11 (2019) 41649–41658.
[33] Y. Alapan, A.C. Karacakol, S.N. Guzelhan, I. Isik, M. Sitti, Reprogrammable shapemorphing of magnetic soft machines, Sci. Adv. 6 (2020) eabc6414.
[34] L. Wang, D. Zheng, P. Harker, A.B. Patel, C.F. Guo, X. Zhao, Evolutionary design of magnetic soft continuum robots, Proc. Natl. Acad. Sci. 118 (2021) 21.
[35] L. Wang, C.F. Guo, X. Zhao, Magnetic soft continuum robots with contact forces, Extreme Mech. Lett. (2022) http://dx.doi.org/10.1016/j.eml.2022.101604.
[36] S. Wu, C.M. Hamel, Q. Ze, F. Yang, H.J. Qi, R. Zhao, Evolutionary algorithm-guided voxel-encoding printing of functional hard-magnetic soft active materials, Adv. Intell. Syst. 2 (2021) 2000060.
[37] F. Dadgar-Rad, M. Hossain, Finite deformation analysis of hard-magnetic soft materials based on micropolar continuum theory, Inter. J. Solids Struct. In Press (2022).
[38] D. Garcia-Gonzalez, Magneto-visco-hyperelasticity for hard-magnetic soft materials: Theory and numerical applications, Smart Mater. Struct. 28 (2019) 085020.
[39] D. Mukherjee, M. Rambausek, K. Danas, An explicit dissipative model for isotropic hard magnetorheological elastomers, J. Mech. Phys. Solids 151 (2021) 104361.
[40] R. Zhang, S. Wu, Z. Qiji, Z. Zhao, Micromechanics study on actuation efficiency of hard-magnetic soft active materials, J. Appl. Mech. 87 (2020) 091008.
[41] D. Garcia-Gonzalez, M. Hossain, A microstructural-based approach to model magneto-viscoelastic materials at finite strains, Int. J. Solids Struct. 208–209 (2021) 119–132.
[42] D. Garcia-Gonzalez, M. Hossain, Microstructural modelling of hard-magnetic soft materials: Dipole–dipole interactions versus Zeeman effect, Extreme Mech. Lett. 48 (2021) 101382.
[43] H. Ye, Y. Li, T. Zhang, Magttice: A lattice model for hard-magnetic soft materials, Soft Matter 17 (2021) 3560–3568.
[44] L. Wang, Y. Kim, G.F. Guo, X. Zhao, Hard-magnetic elastica, J. Mech. Phys. Solids 142 (2020) 104045.
[45] W. Chen, L. Wang, Theoretical modeling and exact solution for extreme bending deformation of hard-magnetic soft beams, J. Appl. Mech. 87 (2020) 041002.
[46] W. Chen, Z. Yan, L. Wang, Complex transformations of hard-magnetic soft beams by designing residual magnetic flux density, Soft Matter 16 (2020) 6379–6388.
[47] W. Chen, Z. Yan, L. Wang, On mechanics of functionally graded hard-magnetic soft beams, Internat. J. Engrg. Sci. 157 (2020) 103391.
[48] W. Chen, L. Wang, Z. Yan, B. Luo, Three-dimensional large-deformation model of hard-magnetic soft beams, Compos. Struct. 266 (2021) 113822.
[49] A. Rajan, A. Arockiarajan, Bending of hard-magnetic soft beams: A finite elasticity approach with anticlastic bending, Eur. J. Mech. A/Solids 90 (2021) 104374.
[50] A.M. Dehrouyeh-Semnani, On bifurcation behavior of hard magnetic soft cantilevers, Int. J. Nonlin. Mech. 134 (2021) 103746.
[51] T.G. Sano, M. Pezzulla, P.M. Reis, A Kirchhoff-like theory for hard magnetic rods under geometrically nonlinear deformation in three dimensions, 2021, arXiv:2106.15189.
[52] D. Yan, A. Abbasi, P.M. Reis, A comprehensive framework for hard-magnetic beams: Reduced-order theory, 3D simulations, and experiments, 2021, arXiv:2106.14878.
[53] G.A. Maugin, Continuum Mechanics of Electromagnetic Solids, North Holland, 1988.
[54] J.C. Simo, A finite strain beam formulation, the three-dimensional dynamic problem. Part I, Comput. Methods Appl. Mech. Eng. 49 (1985) 55–70.
[55] P. Wriggers, Nonlinear Finite Element Methods, Springer, 2008.
[56] J.C. Simo, On a fully three-dimensional finite-strain viscoelastic damage model: Formulation and computational aspects, Comput. Methods Appl. Mech. Engrg. 60 (1987) 153–173.
[57] G.A. Holzapfel, Nonlinear Solid Mechanics, A Continuum Approach, Wiley, 2000.
[58] J.C. Simo, T.J.R. Hughes, Computational Inelasticity, Springer, 1998.
[59] C.C. Foo, S. Cai, S.J.A. Koh, S. Bauer, Z. Suo, Model of dissipative dielectric elastomers, J. Appl. Phys. 111 (2012) 034102.
[60] T. Zhao, J. Cao, X. Li, M. Xia, B. Xue, H. Yuan, A network-based visco-hyperelastic constitutive model for optically clear adhesives, Extreme Mech. Lett. 51 (2022) 101594.
[61] M. Kollosche, G. Kofod, Z. Suo, J. Zhu, Temporal evolution and instability in a viscoelastic dielectric elastomer, J. Mech. Phys. Solids 76 (2015) 47–64.
[62] M. Hossain, Z. Liao, An additively manufactured silicone polymer: Thermo-viscoelastic experimental study and computational modelling, Addit. Manuf. 35 (2020) 101395.